



Unlocking the full potential of Sentinel-1 for flood detection in arid regions

Shagun Garg ^{a,d,*}, Antara Dasgupta ^b, Mahdi Motagh ^{c,d}, Sandro Martinis ^e,
Sivasakthy Selvakumaran ^a

^a University of Cambridge, Engineering Department, Cambridge, United Kingdom

^b RWTH Aachen University, Institute of Hydraulic Engineering (IWW), Faculty of Civil Engineering, Germany

^c Institute of Photogrammetry and GeoInformation, Leibniz University Hannover, Germany

^d GFZ German Research Centre for Geosciences, Department of Geodesy, Section of Remote Sensing and Geoinformatics, Potsdam, Germany

^e German Aerospace Center (DLR), German Remote Sensing Data Center (DFD), Oberpfaffenhofen, Germany

ARTICLE INFO

Keywords:

Flood mapping
SAR
Machine learning
Remote sensing
Coherence
Disaster management

ABSTRACT

Climate change has intensified flooding in arid and semi-arid regions, presenting a major challenge for flood monitoring and mapping. While satellites, particularly Synthetic Aperture Radar (SAR), allow synoptically observing flood extents, accurately differentiating between sandy terrains and water for arid region flooding remains an open challenge. Current global flood mapping products exclude arid areas from their analyses due to the sand and water confusion, resulting in a critical lack of observations which impedes response and recovery in these vulnerable regions. This paper explores the full potential of Sentinel-1 SAR to improve near-real-time flood mapping in arid and semi-arid regions. By investigating the impact of various parameters such as polarization, temporal information, and interferometric coherence, the most important information sources for detecting arid floods were identified. Using three distinct arid flood events in Iran, Pakistan, and Turkmenistan, different scenarios were constructed and tested using RF to evaluate the effectiveness of each feature. Permutation feature importance analysis was additionally conducted to identify key elements that reduce computational costs and enable a faster response during emergencies. Fusing VV coherence and amplitude information in pre-flood and post-flood imagery proved to be the most suitable approach. Results also show that leveraging crucial features reduces computational time by ~35% as well as improves flood mapping accuracy by ~50%. With advancements in cloud processing capabilities, the computational challenges associated with interferometric SAR computations are no longer a barrier. The demonstrated adaptability of the proposed approach across different arid areas, offers a step forward towards improved global flood mapping.

1. Introduction

Floods are one of the most common, widespread, and destructive disasters. Currently, around 23% of people in the world are directly exposed to 1-in-100-year flooding (Rentschler et al., 2022). Almost 90% of those exposed to flooding live in lower or middle-income countries, and this number is only likely to increase as indicated by climate change projections for 2030 (Tellman et al., 2021). In the year 2021 alone, flooding cost the global economy more than \$82 billion, accounting for nearly a third of all losses from natural catastrophes around the globe (Bevere et al., 2023).

Global flood data often underestimate the vulnerability of floods in arid regions, which has become increasingly frequent due to changes in the spatial distribution of precipitation as a result of climate change (Gabellini, 2021). The low permeability of the soil in arid regions means that even short periods of heavy rain can result in rapid surface

runoff, causing erosion and damage to infrastructure (Lin, 1999). The impacts of floods in deserts are exacerbated by the fact that arid regions often lack the infrastructure and resources necessary to cope with such disasters (Network, 2020; Eslamian and Eslamian, 2022). Dams and embankments, often constructed in these regions to respond to heavy rainfall and store water for extended dry periods, have frequently failed due to poor maintenance (Motagh and Akhani, 2023). When breaches occur, the resulting floods are not only fast-moving but also carry a huge amount of sediment, increasing their destructive potential. In addition, many arid regions have rivers that are typically dry or have minimal flow throughout most of the year, known as ephemeral rivers. Intense rain events can abruptly activate these riverbeds, leading to unexpected flooding in areas unaccustomed to such events (Korichi et al., 2016). The projected expansion of arid and semi-arid regions due to climate change, an estimated increase of about 10% each over

* Corresponding author at: University of Cambridge, Engineering Department, Cambridge, United Kingdom.
E-mail address: sg2009@cam.ac.uk (S. Garg).

the next 50 years (Tabari, 2020), demands an urgent development of improved flood monitoring strategies.

1.1. State-of-the-art flood mapping

Satellites have been increasingly used for flood detection because they can cover areas that are often inaccessible during such events. While optical satellites have limitations in penetrating through clouds, Synthetic Aperture Radar (SAR) overcomes this obstacle by providing cloud-free day and night images and has been extensively used in flood mapping (Landuyt et al., 2019; Dasgupta et al., 2018a). In ideal cases, flood maps can be derived by leveraging the contrast between water and non-water areas in SAR imagery (Hein, 2004). Depending on the number of images used, flood detection using SAR data can be broadly classified into three categories: single-image analysis, change detection (CD), and multi-temporal analysis.

In single-image methods, floodwater mapping involves identifying the water class through histogram thresholding (Bereczky et al., 2022; Pulvirenti et al., 2014; Martinis et al., 2015; Chini et al., 2017; Schumann et al., 2022; Schlaffer et al., 2015; Chini et al., 2019; Pulvirenti et al., 2016). A pixel is classified as ‘flooded’ if the backscatter amplitude value falls below a given threshold which ideally separates the bimodal water/non-water amplitude distributions. While this is a rapid technique, it has limitations in dealing with false positives caused by non-flooded land cover classes exhibiting similar backscattering characteristics as water, such as sandy regions and tarmac. The single-image method only extracts smooth open water and does not differentiate between permanent water bodies and floodwater (Chini et al., 2017; Wagner, 2024). CD techniques overcome some of these barriers. By analyzing two SAR scenes acquired within a short temporal baseline, changes in backscatter amplitude values can be attributed to floodwater (Li et al., 2018). This approach reduces false positives caused by other targets with low amplitude values (Ivan Ulloa et al., 2020). Multi-temporal SAR analysis further improves flood mapping by considering a long temporal archive of pre-flood images (DeVries et al., 2020; Vanama et al., 2021b, 2020; Lin et al., 2019).

In addition to backscatter amplitude analysis, several studies have explored the use of interferometric coherence and polarimetric information to improve flood detection. Interferometric coherence, which is a measure of the consistency and stability of the phase relationship between two radar signals, has been utilized to map floodwater in vegetated and urban areas (Brisco et al., 2017; Canisius et al., 2019; DeLancey et al., 2019; Mohammadi manesh et al., 2018a,b; Santoro et al., 2010; Cartus et al., 2022; Santoro et al., 2007; Schumann et al., 2022; Delgado Blasco et al., 2020; Mason et al., 2014; Tay et al., 2020). Polarimetric SAR data, which include multiple polarization channels, have been used to derive additional flood-related information such as surface roughness and vegetation characteristics (Jo et al., 2018; Mahdavi et al., 2019; Adhikari et al., 2023). These improvements have been complemented by machine learning and data analysis techniques to enable more accurate, rapid, and automated flood detection (Ghosh et al., 2022; Li et al., 2019; Zhao et al., 2022; Wu et al., 2023; Yadav et al., 2022a,b; Bovolo and Bruzzone, 2007).

Building on these advancements in flood mapping techniques, the Copernicus Emergency Management Service (CEMS) has developed the systematic operational global SAR-based flood monitoring algorithm that combines three independent floodwater mapping approaches proposed by the Luxembourg Institute of Science and Technology (LIST), the German Aerospace Center (DLR), and the Vienna University of Technology (TU Wien) (Krullikowski et al., 2023; Martinis et al., 2015; Twele et al., 2016; Bauer-Marschallinger et al., 2022). The final floodwater map generated by this algorithm is based on a majority voting system, where at least two algorithms must agree for a pixel to be classified as flooded. The confidence level of the combined product is determined by the arithmetic mean of all likelihoods. The final step includes an exclusion layer to filter out areas where SAR-based flood

mapping is insensitive to surfaces (e.g., urban areas, dense vegetation), low backscatter (e.g., sandy surfaces, flat impervious areas), radar shadows and topographic distortions (Krullikowski et al., 2023). This poses a major challenge in mapping floods in arid regions. Current techniques are found to be inadequate because dry, sandy areas are indistinguishable from water (Martinis et al., 2018). To address this issue and improve overall accuracy, arid regions are excluded from the mapping process, further exacerbating the gap in addressing flood detection and mapping in arid regions (Krullikowski et al., 2023).

1.2. SAR flood detection challenges in arid areas

SAR flood detection in arid regions faces unique challenges due to the similar backscatter characteristics of water and dry sandy surfaces. Backscatter coefficients depend on radar wavelength, surface roughness, and material electrical properties, particularly the dielectric constant (Ulaby et al., 1978; Fatras et al., 2012). In arid regions, soil moisture often determines backscatter amplitude, due to its influence on the dielectric constant (Toca et al., 2022; Ulaby et al., 1996). C-band radar (e.g. Sentinel-1), can penetrate dry sandy soils, complicating moisture retrievals due to sub-surface scattering (Wagner et al., 2013, 2022). However, water-saturated sandy surfaces prevent radar penetration, due to specular reflection or signal attenuation resulting in low backscatter (Prigent et al., 2015; Schaber et al., 1986). This phenomenon creates confusion between water bodies and arid areas in SAR imagery. As illustrated in Fig. 1(a), the optical images clearly differentiate between arid areas, water bodies, and urban areas, but in the corresponding Sentinel-1 SAR image, water and dry arid areas exhibit similar low backscatter (Fig. 1(b); $\mu_{\text{water}} = -19.20 \text{ dB}$; $\mu_{\text{arid}} = -17 \text{ dB}$). In contrast, urban areas appear brighter due to the double-bounce effect and are thus easily distinguishable (Fig. 1(b); $\mu_{\text{urban}} = -6.30 \text{ dB}$). Although water typically exhibits slightly lower backscatter values than dry arid soils due to the absence of sub-surface scattering, the distributions are often too similar to reliably distinguish based on backscatter contrast. This similarity poses a major challenge for SAR-based flood detection in arid regions.

SAR polarization could also play a role in identifying arid floods, as it helps to better understand the shape and structure of the target. Since polarimetric SAR sensors transmit and receive in vertically and horizontally polarized electromagnetic fields, the changes observed in the polarization of waves reflected back from the Earth's surface can be used to better identify surface features. A fully polarimetric SAR system typically measures the complex scattering matrix with quad-polarization, providing amplitude as well as phase information associated with the reflectivity of all the scatterers contained in a ground resolution cell (Yang et al., 2019). The Copernicus Sentinel-1, an open systematic SAR data, is a dual-polarized system and thus, does not offer similar capabilities. Although due to the differences in amplitude as well as phase responses in co-polarized (e.g. VV or vertically sent-vertically received) and cross-polarized (e.g. VH vertically sent-horizontally received), it is worth investigating the differences in arid flood detection capabilities, as it has demonstrated benefits for land cover mapping accuracies (Panahi et al., 2022).

In addition to the challenges posed by similar backscatter characteristics, there is a notable lack of flood mapping datasets for arid regions. Unlike regions that regularly experience floods and have extensive data records, arid regions encounter irregular flooding events, making it challenging to curate a benchmark dataset suitable for arid regions. Recently, a few labeled flood classification datasets such as SEN1Floods11 (Bonafilia et al., 2020), Sen12-FLOOD (Rambour et al., 2020), MMFloods (Montello et al., 2022) and S1S2-Water (Wieland et al., 2023), have included dry regions. Still, the labels are made only by considering amplitude threshold which assumes a clear distinction between water and non-water classes which does not hold for arid regions as discussed above and shown in Fig. 1. Only a few studies have considered SAR-based flood detection in arid regions. Wendleder

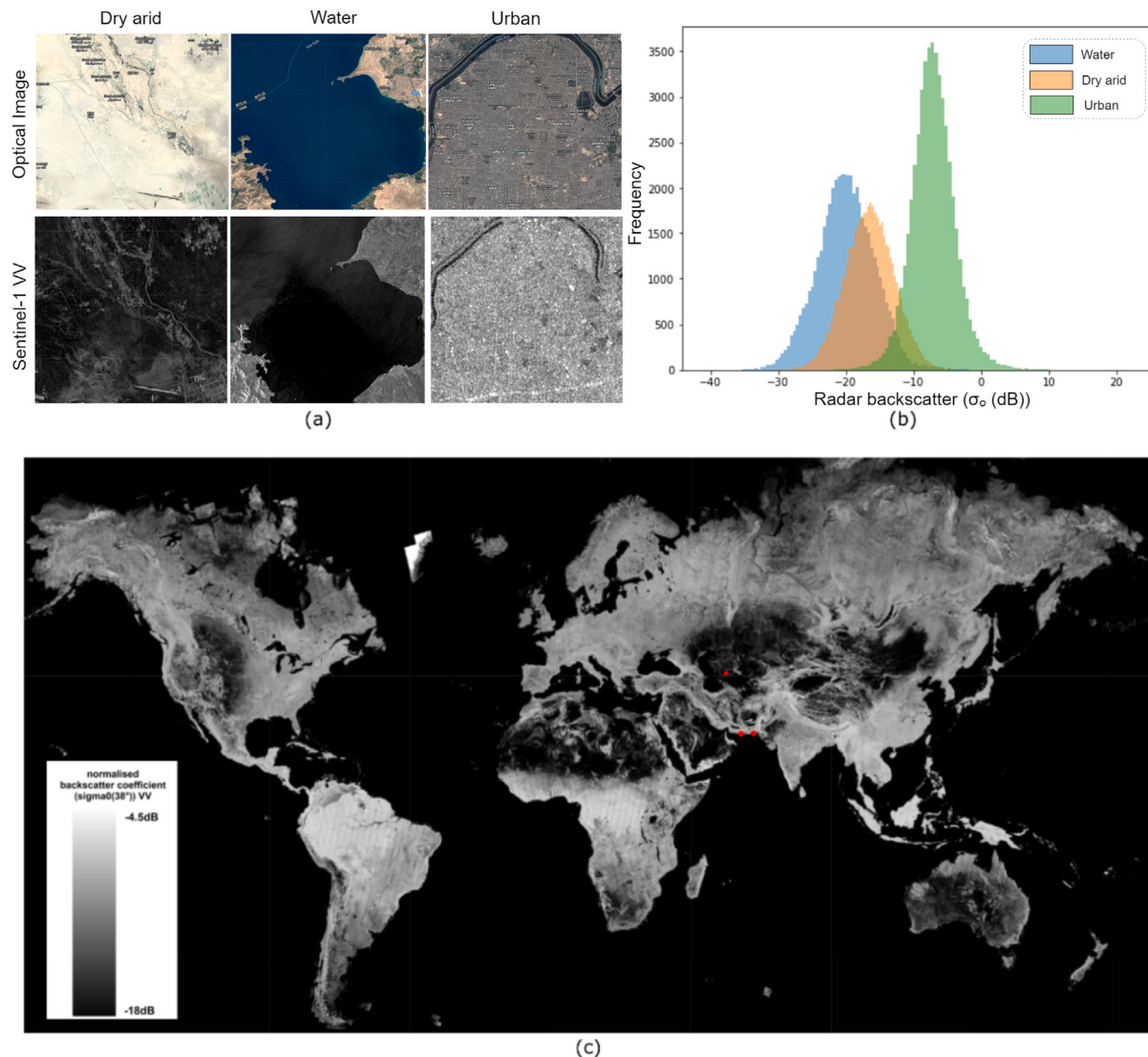


Fig. 1. Fig. 1(a) shows how dry arid regions, water bodies, and urban areas appear in high-resolution Maxar optical imagery from Google Earth (top row) and Sentinel-1 SAR imagery in VV polarization (bottom row). In the optical imagery, it is easy to distinguish between dry regions, water, and urban areas, but in the SAR imagery, dry arid regions and water appear similar. Fig. 1(b) illustrates the VV backscatter frequency distributions of Sentinel-1 VV pixels for water, dry arid, and urban areas. Fig. 1(c) displays the Sentinel-1 Global Mean Backscatter (Bauer-Marschallinger et al., 2021) in VV polarization, providing a visual representation of the arid regions of the world exhibiting low mean backscatter throughout the year. The red points show the study sites chosen in this paper. (For interpretation of the references to color in this figure legend, the reader is referred to the web version of this article.)

et al. (2013) used the Moderate Resolution Imaging Spectroradiometer (MODIS)/Terra Land Cover Types dataset and a global water indication mask (WAM) to exclude desert regions. Another study by Bertram et al. (2016) utilized a lake extent mask to account for water look-alikes from dry sand surfaces during long-term monitoring dynamics of Lake Tabalak in the West-African Sahel region. Two notable studies addressed the exclusion of arid areas based solely on SAR data. First, Martinis et al. (2018) proposed the Sand Exclusion Layer based on the temporal backscattering Sentinel-1 dataset to address the challenge of arid areas that exhibit consistently low backscattering values, which could potentially be misidentified as water bodies. Zhao et al. (2021) extended this approach and generated exclusion maps (EX-map) for radar shadows and arid regions combined with other water-look-alike places based on temporal SAR statistics.

Although exclusion layers improve the overall flood mapping accuracy, they do so by ‘excluding’ the so-called sensitive areas from

the processing, which in this research context consists of dry or sandy areas. Therefore, if a flood occurs in these areas the current Sentinel-1 amplitude-based techniques provide no information on these areas. In the context of climate change and increased flooding in dry areas, it is necessary to address this limitation. A clear example of this can be seen in Fig. 1(c), which shows the global mean backscatter derived using Sentinel-1 (Bauer-Marschallinger et al., 2021). This Figure illustrates how some parts of Northern Africa, the Middle East, and Australia have a backscatter very similar to that of water, making it difficult to distinguish between water and land, and are hence usually excluded from the processing. To refine SAR-based flood detection, Ritusree et al. (2023) explored the SAR texture information for arid flood detection. Although promising, integrating texture is computationally intensive and has scalability issues. The application of SAR texture in flood mapping remains largely unexplored, and further research is needed to identify which specific texture features and parameters most effectively improve detection results (Dasgupta et al., 2018b).

1.3. The potential of interferometric coherence

Coherence, denoted by γ , is a product of multiple correlation terms, each contributing to overall decorrelation:

$$\gamma = \gamma_{\text{proc}} \gamma_{\text{geom}} \gamma_{\text{vol}} \gamma_{\text{SNR}} \gamma_{\text{temporal}} \quad (1)$$

Here, γ_{proc} are changes in coherence due to processing, γ_{geom} refers to geometric decorrelation, γ_{vol} denotes volume decorrelation, while decorrelation due to noise by γ_{SNR} , and γ_{temporal} refers to decorrelation due to surface changes. Understanding the impact of all factors is crucial for correctly identifying decorrelation due to surface changes from flooding. A study by Schepanski et al. (2012) leveraged Envisat ASAR interferometric coherence information to improve flood detection in dry valleys. They found that although coherence shows promise in delineating flood extents in arid valleys, there are limitations related to the specific operational parameters of the Envisat sensor, such as viewing geometry and large orbital baselines which led to coherence losses that were not necessarily related to flooding.

The use of Sentinel-1 data, in combination with advanced algorithms, has mitigated some of these issues. Processing errors, such as misalignments in coregistration, can negatively affect coherence quality (Haiqin et al., 2013), but the use of streamlined Sentinel-1 processing algorithms has reduced these errors. Geometric decorrelation, which arises from differences in satellite positions during acquisitions, is negligible due to the stable orbits of Sentinel-1 satellites (Geudtner et al., 2014). Volume decorrelation, caused by multiple scatterers within a pixel such as dense vegetation, generally has less impact in barren arid regions (Abdel-Hamid et al., 2021; Wang et al., 2010). Signal-to-noise (SNR) decorrelation, which can be estimated using the Noise equivalent sigma zero information from Sentinel-1 metadata, is also effectively mitigated by the use of Sentinel-1 data and advanced algorithms (Piantanida et al., 2017).

For flood mapping, the primary focus is on temporal decorrelation (γ_{temporal}), which represents decorrelation caused by changes over the time interval between SAR acquisitions. Events such as flooding cause the signal to decorrelate and causes a drop in coherence. Given the benefits of Sentinel-1, including stable baselines and higher resolution, further research that takes advantage of the full potential of Sentinel-1 could provide valuable contributions to flood mapping in arid regions.

1.4. Research questions and scope

The study focuses on flood mapping challenges in arid regions during specific real-world flood events. The following research questions guided the comprehensive analysis:

1. What role do different polarizations play in mapping floods in arid regions?
2. Can combining amplitude and coherence data improve the accuracy of flood classification in arid regions?
3. Does including pre-flood event information enhance the effectiveness of flood mapping in arid regions?
4. How can we optimize for computational efficiency, accuracy, and explainability towards operational arid flood mapping?

In doing so, we explored potential polarization, phase, and temporal information using publicly available Sentinel-1 data. To validate the results, we utilized Sentinel-2 data. This paper introduces three notable contributions to the field of flood mapping from SAR. Firstly, our approach stands out for its self-consistency by relying only on SAR data. While we utilize additional datasets for validation purposes, our flood mapping methodology does not depend on them. This is particularly useful in situations where optical data may not be readily available (e.g., due to cloud cover). Secondly, and for the first time, we address flooding in arid regions using SAR and attempt to improve it in contrast to its ‘exclusion’ in previous literature. Lastly, our research aims to

identify the most optimal features for flood mapping. We consider factors such as quick response time, reduced computational cost, and ease of interpretation. The insights from this SAR-based flood mapping study are valuable for developing future global floodwater mapping algorithms, especially for often overlooked arid regions.

2. Data and study areas

2.1. SAR and multispectral dataset

The Sentinel-1 A and Sentinel-1B satellites used in this study operate at C-band SAR (frequency 5.404 GHz; wavelength 5.54 cm). They were the first among a series of Earth Observation (EO) satellite programs launched by the European Space Agency (ESA) Copernicus program. Sentinel-1 A was launched in April 2014 followed by Sentinel-1B in April 2016. Each of the two satellites orbits the earth every 12 days, creating a joint constellation repeat cycle of 6 days over the equator (the repeat cycle increased to 12 days since the failure of Sentinel-1B in December 2021, but it is expected to be restored to 6 days with the launch of the Sentinel-1C). Two different product types of Sentinel-1 data were acquired using the Alaska Satellite Facility (ASF) DAAC services: (1) Single Look Complex (SLC) for interferometric coherence generation, and (2) Ground Range Detected (GRD) for amplitude information in VV and VH polarizations. The datasets were then processed for flood mapping (discussed in Section 3).

The Sentinel-2 satellite constellation operated by ESA in the framework of the Copernicus program provides the highest spatial resolution multispectral remote sensing data openly and freely available to the public. It consists of two polar-orbiting satellites at an altitude of 786 km and is equipped with a multispectral imager that captures 13 spectral bands with a width of 290 km. The ground resolution of the data ranges from 10 m to 60 m, and the satellite has a revisit period of ten days for one satellite and five days for two complementary satellites. Due to different spectral responses from water/land areas, the following spectral bands were used: blue (B2), green (B3), red (B4), near-infrared (B8) at 10 m spatial resolution, short-wave infrared 1 (B11), and short-wave infrared 2 (B12) at 20 m spatial resolution. Google Earth Engine (GEE) hosts Sentinel-2 level-2 A orthorectified atmospherically corrected surface reflectance data which was used to visualize and download the images chosen to make reference masks and validate the model results.

2.2. Ancillary datasets

The Environmental Systems Research Institute Land Use/Land Cover Database (ESRI LULC 2019) was utilized for land cover information (Karra et al., 2021). This dataset provides a time series of annual global maps of land use and land cover, generated through the application of the ESA Sentinel-2 data. The dataset consists of composite maps from 2017 to 2021 and provides land use and land cover predictions for nine different classes. The analysis of the study areas focused on five primary land cover classes: bare land, range land, urban areas, crops, and water. We used the global land European Digital Elevation Model (COP-DEM) for the topography information. It was made available in 2020 through ESA and is based on high spatial resolution commercial SAR data acquired during the TanDEM-X Mission (Li et al., 2022). It integrates detailed terrain corrections and hydrological adjustments, including the elimination of spikes, holes, and implausible terrain structures, as well as shoreline corrections and random bias corrections (Li et al., 2022).

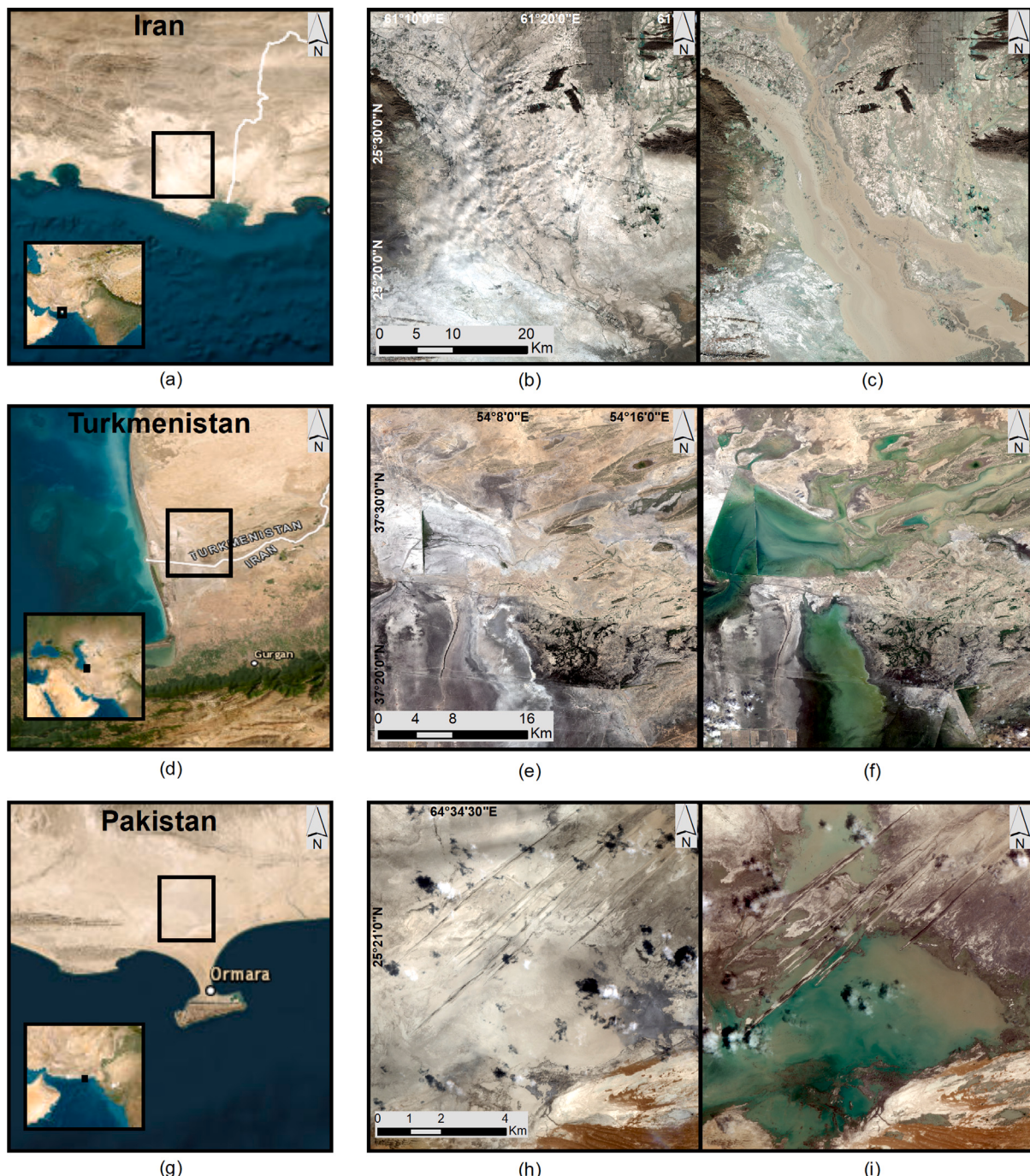


Fig. 2. Case studies: Distinct geographical locations and their associated flood events — Sistan, Iran (a), Esenguly, Turkmenistan (d), and Ormara, Pakistan (g). Each area's high-resolution satellite data displayed in Google Earth is shown in the first panel (a, d, and g) respectively. The second and third panels represent pre-flood and post-flood Sentinel-2 images respectively. Notably, each region reveals different levels of water turbidity during flooding, with full turbidity in Iran and partial turbidity in Pakistan and Turkmenistan. The respective imagery was captured on 8th January 2020 and 13th January 2020 for Iran; 16th March 2019 and 10th April 2019 for Turkmenistan; and 2nd August 2020 and 14th August 2020 for Pakistan. (At first glance, the subplot 'b' appears to be heavily obscured by cloud cover. However, closer inspection at the pixel level reveals that the clouds are relatively thin, allowing visualization of the underlying landscape before flooding.)

2.3. Study site selection and case studies

The selection of appropriate study sites was a key aspect of our research, given the tendency in flood mapping to use stable water bodies such as lakes or rivers for flood mapping model training due to their clearly defined boundaries (Wieland et al., 2023). However, our study highlights a crucial distinction: In arid regions, floodwaters often carry debris and can be shallow, affected by objects resting on the ground, making the water surface rough. This differs from the clearer,

deeper waters of stable bodies, affecting backscattering and spectral signatures. For this reason, our objective was to cover flood events in arid areas captured by optical and SAR datasets, ensuring a more accurate reference map from optical data. Initial reliance on EO-based disaster services such as The International Charter “Space and Major Disasters” ([Charter](#)), CEMS ([CEMS](#)), and the Sentinel Asia (a United Nations Office for Outer Space Affairs international cooperation platforms for disasters management in the Asia-Pacific region) ([Sentinel-Asia](#)) revealed a gap in the mapping of suitable arid regions, often limited by

Table 1

Table provides the acquisition dates of Sentinel-1 and Sentinel-2 satellite imagery used for analyzing pre-flood and post-flood events across three case studies. The third column details the Sentinel-2 surface reflectance (L2A) product, while the fourth column lists the Sentinel-1 GRD acquisition dates. The fifth column specifies the Sentinel-1 SLC data used for coherence generation. Note that the post-flood imagery is chosen on the same day for both Sentinel-2 and Sentinel-1 datasets (e.g., 13-Jan-2020 for Iran, 10-Apr-2019 for Turkmenistan, and 14-Aug-2020 for Pakistan). This is crucial for accurate validation of the flood extent. For terminology, refer to [Table 2](#).

		Sentinel-2 L2A Bands 2–4, 8, 11, 12	Sentinel-1 GRD VV & VH	Sentinel-1 SLC VV & VH
Iran	post-flood	13-01-2020	13-01-2020	01-01-2020 & 13-01-2020
	pre-flood	08-01-2020	01-01-2020	20-12-2019 & 01-01-2020
Turkmenistan	post-flood	10-04-2019	10-04-2019	17-03-2019 & 10-04-2019
	pre-flood	16-03-2019	17-03-2019	05-03-2019 & 17-03-2019
Pakistan	post-flood	14-08-2020	14-08-2020	02-08-2020 & 14-08-2020
	pre-flood	02-08-2020	02-08-2020	21-07-2020 & 02-08-2020

the use of SAR amplitude data to generate flood maps or the absence of concurrent high-resolution optical imagery.

To account for this, we curated new datasets focused on arid flood events with both SAR and optical data available on the same day, enhancing the reliability of our flood maps. We chose Sentinel-1 and Sentinel-2 data for their public and free availability. The search was narrowed to events with ‘cloud-free’ Sentinel-2 images that coincided with Sentinel-1 data, substantially reducing the pool of potential case studies but ensuring data quality. This rigorous selection process led to the identification of three distinct regions worldwide, each presenting a different flooding type. The details of the images and datasets for these study areas are summarized in [Fig. 2](#) and [Table 1](#). [Table 2](#) defines the terms used in this paper for broader accessibility.

- 1. Flash flooding in Sistan, Iran in January 2020 :** severe rain events in January caused multiple dams to overflow in the province of Sistan-Baluchestan, resulting in widespread flooding ([FloodList](#)). The flooding broke the check-dams which led to major damage downstream in agricultural lands and residential areas. Insufficient maintenance of flood protectors contributed to the severity of the flooding ([Peyravi et al., 2019](#)).
- 2. Dam break in Esenguly, Turkmenistan in April 2019 :** A low-pressure system in early March 2019 caused heavy precipitation, and subsequent dam failure was reported on the Etrek river in Turkmenistan. This resulted in flooding in the rural areas of Esenguly in Balkan Velayat. Limited information is available about this event, but it impacted lives and infrastructure due to challenges in access and communication with affected communities ([Smiljanic et al., 2019](#)).
- 3. Heavy rainfall in Ormara, Pakistan in August 2020 :** In southwest Pakistan, heavy monsoon rainfall led to flooding and extensive damage. Ormara in the Gwadar District, a region dominated by desert and exposed rocks, experienced significant impacts with 8 casualties, numerous missing individuals, and the destruction of over 140 homes. Notably, Ormara recorded 88 mm of rain in 24 h on August 8, 2020, according to the Pakistan Meteorological Department (PMD) ([Pak Mission Society, 2020](#)).

3. Methodology

The data-processing workflow and related steps included in this framework are outlined in [Fig. 3](#), and discussed in detail in this section. All EO datasets, after post-processing, were reprojected into the WGS84 latitude/longitude projection (EPSG:4326).

3.1. Reference flood mask generation

The accuracy of our model was validated using a reference dataset of flood masks derived from Sentinel-2 images. To maximize the comparability of the flood maps, we ensured that Sentinel-2 images corresponded to the same dates as the Sentinel-1 images, which strongly

Table 2

Clarification of flood-event terminology used in this study.

Term	Definition
pre-flood	Image acquired before the flood event.
post-flood	Acquired during the flood event, where the flood extent is visible in the image.
co-flood	Image pair: one pre-flood and one during-flood event.

limited the number of case studies available for this study. In arid regions, the high sediment content in floodwater makes it difficult to detect flooding in optical images. To address this, we inspected all available Sentinel-2 bands, identifying those with the most noticeable spectral changes post-flood. For visualization, we used Sentinel-2 bands B3 (green), B8 (near-infrared) and B11 (short-wave infrared) and applied a modified Normalized Difference Water Index (MNDWI) as proposed by [Xu \(2006\)](#). Given the bimodal nature of the histogram, the Otsu method was used for automatic thresholding ([Otsu, 1979](#)), which determines the optimal threshold by maximizing the variance between the two classes. In all cases, the threshold value was consistently found to be -0.22. The flood masks were manually cleaned to remove obstructions caused by the clouds or their shadows. In instances where smaller clouds were present within water bodies, these were classified as water. Conversely, in cases where cloud shadows intersected with water bodies, we labeled these pixels as no-data, thereby excluding them from subsequent processing. The final mask developed consisted of three classes: water, land, and no data.

Despite these efforts, we recognize that certain uncertainties persist, particularly along the flood boundary. Proper flood boundary delineation is a complex task even under optimal conditions and using high-resolution optical imagery. It is even more complicated in sediment-heavy turbid flood waters, which is normal in arid regions. Nevertheless, we strived to achieve the highest possible accuracy in our reference flood mask through careful area selection and manual post-processing. It is important to note here that the purpose of the cloud-free optical images used in this study was to test the accuracy of our methodology. The practical application of this research will not require optical images.

3.2. Sentinel-1 SAR data pre-processing

3.2.1. Sentinel-1 amplitude

Sentinel-1 GRD datasets are pre-processed focused SAR datasets from raw single-look complex imagery, multi-looked, and projected to ground range using the WGS84 ellipsoid model. The output is produced with square pixels, each pixel representing the detected amplitude. In our study, we processed these GRD datasets into radiometric terrain corrected (RTC) products to mitigate terrain-induced backscatter variations. Initially, orbit file corrections from the Copernicus Precise Orbit Determination (POD) Service refined the positioning data. Then, we removed thermal noise and edge artifacts in GRD datasets to eliminate

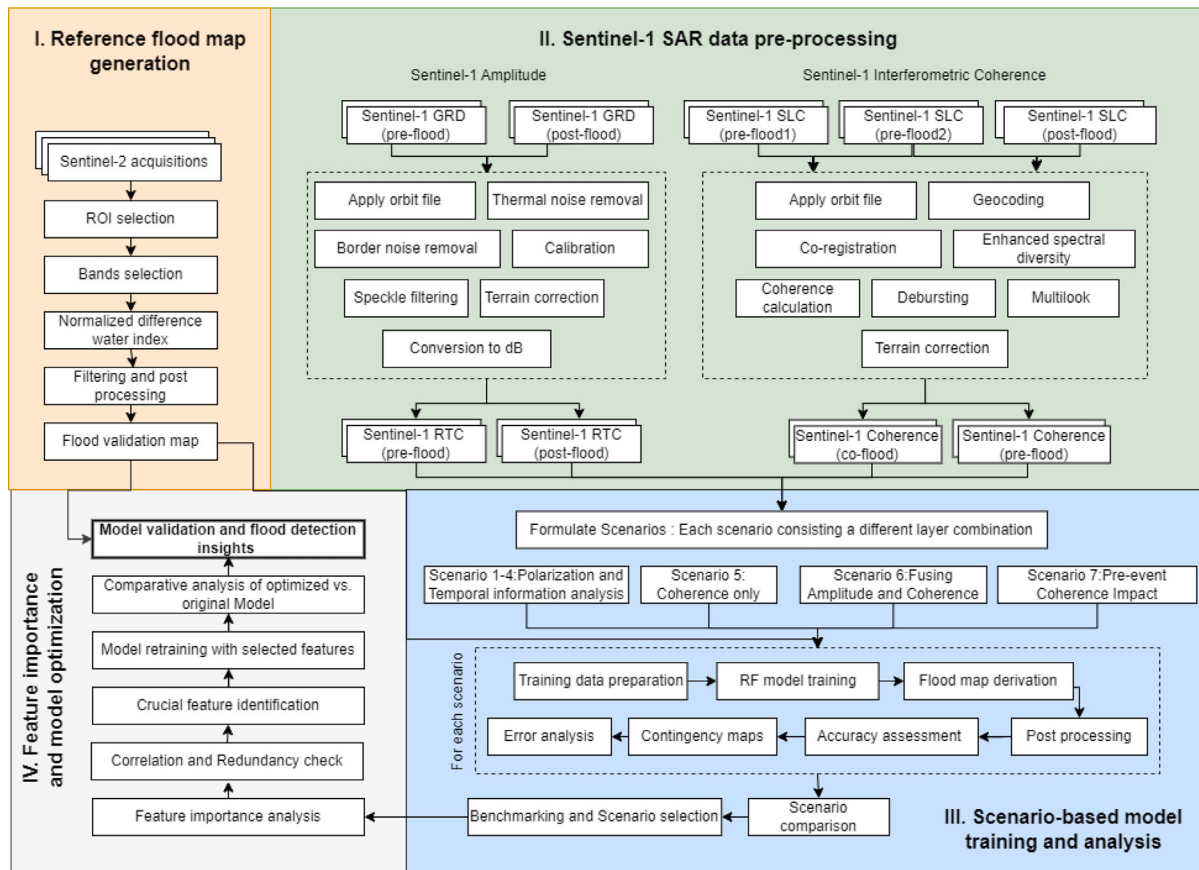


Fig. 3. Methodology is divided into four comprehensive blocks, with each block detailed in Section 3. The block ‘Model validation and flood detection insights’ is highlighted (in bold) as it represents the end of the flowchart.

spurious pixel values not marked as ‘NODATA’. Following noise correction, we calibrated the product to transform digital pixel values into radiometrically calibrated backscatter coefficients. We then applied the Lee Sigma speckle filter (Lee et al., 2009) to minimize speckle noise, enhancing image clarity. Given SAR side-looking geometry, signal distortions occur over varied elevations, such as mountainous areas, leading to image geometric distortions (Hein, 2004). To correct these, terrain adjustments using Copernicus 30 m global DEM was applied, reducing geolocation errors from such distortions (Li et al., 2022). The final step involved transforming the unitless backscatter γ_{int} into decibels (dB) through logarithmic conversion, as detailed in Eq. (2), to standardize the backscatter measurements for analysis. The processing was done using ESA SNAP toolbox.

$$\gamma_0(\text{dB}) = 10 \log_{10}(\gamma_{\text{int}}) \quad (2)$$

3.2.2. Sentinel-1 interferometric coherence generation

Sentinel-1 SLC products provide two types of information: amplitude of the backscatter signal and complex phase information. Phase information is however lost while converting SLC to GRD products. To utilize the phase information, SLC images were processed to estimate coherence using a technique known as interferometry. Interferometric SAR (InSAR), well known for its use in mapping surface deformation (Karanam et al., 2021; Garg et al., 2022), has also been explored in the flood mapping domain over the years (Chini et al., 2019). InSAR involves the comparison of two or more SAR images covering the same extent. By analyzing the phase differences between the images, changes in the ground surface can be detected. However, it is crucial to select pairs with short temporal baselines to ensure that changes mainly reflect the flooding areas, minimizing other variations. In our study, we produced two coherence maps: a co-flood coherence map

derived from images taken immediately before and during the flood event, and a pre-flood coherence map from images before the flood. For both maps, we utilized a 12-day interval period between acquisitions to ensure temporal proximity and relevance.

To generate coherence, SLC products were downloaded from the ASF and processed using the ESA SNAP toolbox. First orbit files were applied to SLC SAR images and then the specific swaths and bursts in which our region of interest lies were selected using the ‘Topsar Split’ operator. Two Sentinel-1 SLC split datasets with a temporal baseline of 12 days were selected and co-registered to align SAR images and facilitate pixel-to-pixel matching for accurate phase differencing (Li and Bethel, 2008). Coregistration was conducted using a Copernicus 30 m global DEM-assisted ‘back-geocoding’ operator using cross-correlation analysis. This cross-correlation analysis provided insights into the remaining offsets in both range and azimuth dimensions for each image pair undergoing co-registration (Wegmuller, 1999). In general, the observed offsets were typically within a range of ± 0.02 pixels in azimuth and mostly within ± 0.1 pixels in range. These minimal offsets strongly support the accuracy of the orbit information provided by Sentinel-1, which facilitates achieving a co-registration accuracy that effectively maintains coherence (Krieger et al., 2007).

Once the pixels in the SAR image pair are aligned and co-registered, the magnitude of the complex cross-correlation coefficient can be computed as shown in Eq. (3)

$$\gamma = \frac{\langle s_1(x, y)s_2(x, y)^* \rangle}{\sqrt{\langle |s_1(x, y)|^2 \rangle \langle |s_2(x, y)|^2 \rangle}} \quad (3)$$

where γ is the coherence value at pixel location (x, y) , s_1 and s_2 are the complex values of SLC images 1 and 2 at pixel location (x, y) , and $*$ stands for the complex conjugation. The spatial averaging (marked

Table 3

Table outlines various scenarios, each incorporating a different layer stack. The following are represented: VV pre-flood image (VV Pre), VH pre-flood image (VH Pre), VV post-flood image (VH Post), VH post-flood image (VH Post), co-flood Coherence in VV polarization (Co-Coh VV), co-flood Coherence in VH polarization (Co-Coh VH), pre-flood coherence in VV Polarization (Pre-Coh VV), and pre-flood coherence in VH Polarization (Pre-Coh VH). The presence of a checkmark indicates the inclusion of those layers in the relevant scenario. The 'Research Questions' column associates each scenario with the research questions it addresses.

	VV Pre	VH Pre	VH Post	VV Post	Co - Coh VV	Co - Coh VH	Pre - Coh VV	Pre - Coh VH	No. of layers	Research questions
Scenario 1			✓	✓					2	RQ3
Scenario 2		✓	✓						2	RQ1
Scenario 3	✓				✓				2	RQ1
Scenario 4	✓	✓	✓	✓					4	RQ1, RQ2, RQ3
Scenario 5					✓	✓			2	RQ2
Scenario 6	✓	✓	✓	✓	✓	✓			6	RQ2, RQ3
Scenario 7	✓	✓	✓	✓	✓	✓	✓	✓	8	RQ3, RQ4

by ⟨⟩) was processed over a window of 3 pixels in range and 10 pixels in azimuth direction. Coherence varies from 0 (decorrelated signals) to 1 (perfectly correlated signals). The coherence products from separate bursts were then merged seamlessly into a single image. Generally, the coherence image appears speckled with inherent speckle noise. To reduce this inherent speckled appearance, a multi-look factor of 4 pixels in range and 1 in azimuth direction was applied. Finally, the coherence map was corrected for terrain distortions using Copernicus 30 m global DEM.

3.3. Scenario-based model training and analysis

Our study designed seven scenarios to address specific research inquiries, as outlined in Table 3, which also maps these scenarios to their corresponding research questions. Scenarios 1–4 explored the effects of polarization and the inclusion of pre-flood amplitude information in arid flood mapping, with particular focus on VH polarization in Scenario 2, VV polarization in Scenario 3, and a combination of both in Scenario 4. Scenarios 5 and 6 focused on the impact of coherence, integrating amplitude and coherence data in Scenario 6. Scenario 7 investigated the potential improvement in flood mapping accuracy by adding pre-flood coherence information.

Each scenario was classified using a Random Forest (RF) model trained separately, to understand which input features best support arid flood detection. Our choice of the RF model for flood mapping was influenced by several factors. With limited data from a few case studies, we needed a method offering control and intrinsic interpretability. Unsupervised methods were tested but were unable to identify and explain the complex flood patterns in arid regions, and deep learning methods, while powerful, required more data and offered less interpretability. RF, a supervised machine learning algorithm, was ideal due to its proven effectiveness in remote sensing with limited data (Belgiu and Drăguț, 2016). It has been widely adopted in a variety of remote sensing applications due to its fast processing, accuracy, and ease of result interpretation (Belgiu and Drăguț, 2016). RF is based on the concept of 'ensemble-learning' which is a process of combining multiple learning algorithms to achieve higher predicted performance (Hastie et al., 2009a).

In RF the learning algorithms are several decision trees, which predict whether a data point belongs to the flood class or not in our case. The class selected by most trees is predicted as the final output of the RF classifier through majority voting. The RF model was implemented using the scikit-learn library in Python. The forest was constructed with 100 trees (`n_estimators=100`), a common choice for balancing efficiency and performance (Oshiro et al., 2012). The trees were allowed to grow to their full depth without imposing a limit, an approach that performs well with high-dimensional data (Scorinet, 2017). Default values were used for other parameters, including the minimum number of samples required to split an internal node (`min_samples_split=2`) and the minimum number of samples at a leaf node (`min_samples_leaf=1`), suitable for a wide range of problems and to prevent overfitting (Probst et al., 2019). For splitting nodes in the

decision trees, the Gini impurity criterion was used, effective for binary classification tasks like flood mapping (Breiman et al., 1984).

Our study included three arid flooding case studies. For each case study, we implemented seven scenarios (Table 3) to investigate input feature combinations. Each scenario within a case study was treated independently, with its own RF model trained and validated. For each scenario, both training and testing samples were derived from the same case study, ensuring consistency in the data used for model development and evaluation. We used RF's efficacy with limited training data (Hastie et al., 2009a) for robust testing. Following remote sensing practices (Colditz, 2015; Albertini et al., 2024; Deng and Wu, 2013), we curated a balanced subset of flood and non-flood pixels for training. A sensitivity analysis determined the optimal number of training pixels (Colditz, 2015). For all three case studies and scenarios, less than 1% of the total pixels were sufficient for training, with performance plateauing beyond this point (refer to Figs. A.1, A.2, A.3).

To ensure model reliability and mitigate overfitting, we implemented 10-fold cross-validation (Maxwell et al., 2018). The training data was divided into 10 subsets, with 9 used for training and 1 for validation in each iteration. This process was repeated 10 times, ensuring each subset served as the validation set once. The final model performance metrics represent the average across these iterations. The trained model was then applied to the remaining 99% of the dataset (test dataset), providing a comprehensive evaluation of its performance and enhancing the reliability of the results. The resulting flood map was post-processed to remove isolated pixels and then cross-compared with the reference flood map.

To evaluate the performance of trained models, the five most popular binary accuracy metrics used in image segmentation literature were deployed. These are Overall Accuracy (OA), Producer Accuracy (PA) and User Accuracy (UA) for the flood class, Intersection over Union (IOU), and F1 score, for which the equations and descriptions are provided in Table 4. In the table 'tp' refers to true positives representing water pixels correctly identified as water; true negative (tn) refers to the number of land pixels correctly identified as land; false positives (fp) represent land pixels misclassified as water; and water pixels incorrectly classified as land are false negatives (fn) (Dasgupta et al., 2018b).

In the flood mapping context, OA as a global metric measures the model's overall correctness in detecting flood and non-flood areas. For the flood class specifically, PA quantifies the model's ability to correctly identify actual flood areas, while UA reflects the precision of detected flood areas. The F1 score balances precision and recall for flood detection, while the IOU calculates the overlap ratio between predicted and actual flood areas. Higher values in these flood class metrics indicate better model performance in identifying flooded regions. Here, the output of performance metrics does not represent a ground-truth validation but rather a cross-comparison between the same-day Sentinel-2 flood mask and the model segmentation results.

Table 4
Performance metrics: formulas and descriptions.

Equation	Description
$OA = \frac{tp+tn}{tp+tn+fp+fn}$	Overall accuracy: measures the proportion of correctly predicted water pixels.
$PA = \frac{tp}{tp+fp}$	Producer accuracy: proportion of actual water pixels correctly identified.
$UA = \frac{tp}{tp+fn}$	User accuracy: proportion of predicted water pixels that are accurate.
$F1 = 2 \times \frac{PA \times UA}{PA + UA}$	F1 score: harmonic mean of producer and user accuracies.
$IOU = \frac{tp}{tp+fp+fn}$	Intersection over Union: measures the overlap between the model output and the reference.

3.4. Feature importance and model optimization

Understanding how a machine learning model works is crucial for transparency in decision making. One way of obtaining insight into the workings of a model is through ‘feature importance’. In this study, we used a combination of scenario construction and model retraining along with Permutation Feature Importance (PFI) as multiple methods are recommended for a robust estimation of variable importance (Hooker et al., 2021). PFI measures how much a feature matters to model accuracy, to interpret the most important inputs to the classifier. We do this by checking how accurate the model is with and without the feature being replaced by noise (Altmann et al., 2010). If the model becomes less accurate after the shuffling, it means that the feature is important. However, if the accuracy remains largely unchanged, it suggests that the feature is not that crucial. Mathematically, if the original accuracy is A_o and accuracy after shuffling the feature is A_p , the change is:

$$\Delta = A_o - A_p \quad (4)$$

A larger Δ value indicates that the feature is more important. Given the inherent randomness of this process, which could lead to varied outcomes (Altmann et al., 2010), we performed the shuffling procedure ten times per feature and calculated the average Δ to stabilize the measure. We implemented PFI on the test set to discern the features that are most effective in predicting unseen data. However, it is crucial to acknowledge that PFI does not consider the correlation between features. This means that a low value of Δ might not necessarily indicate a lack of importance but could instead suggest the presence of another feature that is highly correlated and compensates for the shuffled feature, thus diluting the apparent importance between the correlated features. Moreover, random shuffling can lead to physically unrealistic data instances, which may never be observed in real cases. Therefore, we concurrently analyzed feature correlations, to provide a more rounded understanding of the model’s behavior.

Following the PFI assessment, crucial features were identified by iterative testing, focusing on their impact on the accuracy of the model. The model was then retrained using these selected features to investigate its efficiency and accuracy. To assess the impact of optimization, we performed a comparative analysis between the optimized and the original all-layer stack models. This evaluation focused on computational efficiency, including training and prediction times, and overall model accuracy to confirm the optimization’s benefits and establish the practical usability of the refined model in real-world settings.

4. Results

Fig. 4 showcases the images used for analysis for the three case studies. In each case, the first column displays Sentinel-2 RGB images (band4/3/2) before (S2 pre) and after (S2 post) the flood event. The second and third columns show Sentinel-1 amplitude data in VH and VV polarizations for pre-flood (VH Pre and VV Pre) and post-flood scenarios (VH Post and VV Post), respectively. The fourth and fifth columns illustrate pre-flood coherence and co-flood coherence in VH (Pre CohVH and co-flood VH) and VV polarizations (Pre CohVV and co-flood VV) respectively. Sentinel-2 images were used as reference, while Sentinel-1 datasets were used for the experimental design.

We designed several distinct scenarios involving different layer combinations (Table 3) to explore the influence of coherence, polarization, and pre-flood information on flood mapping in arid regions. The results for Iran, Turkmenistan, and Pakistan are presented in Figs. 5, 6, 7 respectively. Each of these Figures consists of 10 images. Images (a) and (b) in the first-row show pre-flood and post-flood images in a false color composite (B8/B11/B12) while (c) displays the ESRI 2019 land cover map (Karra et al., 2021). In images (d) to (j), model predictions from different scenarios are compared with the Sentinel-2-derived reference flood map. White represents land correctly identified as land (true negative), while blue signifies accurately predicted flooded areas (true positive). Red indicates false positives/over-predictions, where the model incorrectly predicted land as flooding and black denotes misses or under-predictions, where actual flooded areas were mistakenly classified as land. The radar chart in Fig. 8 quantitatively assesses the performance of each scenario using accuracy metrics such as OA, PA, UA, IOU, and the F1 score discussed in Table 4. In this plot, the closer a line is to the edge, the higher the metric value, providing an immediate visual comparison of the effectiveness of the scenario.

4.1. Impact of polarization

To explore the impact of polarization on CD accuracy, we designed two distinct scenarios: Scenario 2, which utilized VH polarization, and Scenario 3, which focused on VV polarization. A key observation from comparing these scenarios is the considerable reduction of both overestimations (depicted in red) and underestimations (shown in black) in the VV CD approach, as evidenced across all three case studies (as seen in panels ‘e’ and ‘f’ in Figs. 5, 6, and 7). This improvement can be seen by comparing the yellow (Scenario 2) and black lines (Scenario 3) in Fig. 8 panels a–c, which show a visible increase in all measured metrics. Quantitatively, the transition from VH to VV CD led to substantial improvements: the IOU increased by 50%, 16% and 21%, while the F1 score improved by 13%, 10%, and 12% in the case of Iran, Turkmenistan and Pakistan, respectively.

Integrating both polarizations in Scenario 4 resulted in a further small improvement in the accuracy metrics, as evident in the radar plot (Fig. 8a–c: the red line is slightly higher than the black line, <4% IOU improvement is visible in all study areas). In the Iran case study (Fig. 5 subplots ‘f’, and ‘g’), minor reductions in overestimations around the bottom center are visible, while in the other two case studies, Turkmenistan and Pakistan, there are no noticeable visual differences when adding VH pre-flood and post-flood to the VV CD approach (Scenario 3 vs. Scenario 4; subplots ‘f’, and ‘g’ in Figs. 6 and 7) respectively.

4.2. Impact of coherence

The impact of coherence was first assessed through standalone benchmarking against the amplitude information in arid flood detection accuracy. In comparing Scenarios 4 (Amplitude) and 5 (Coherence) in Iran, a notable reduction in under-predictions can be observed (black regions in Fig. 5‘g’ and ‘h’), alongside a substantial increase in over-predictions, particularly in the upper parts (red regions in Fig. 5‘g’ and ‘h’). The radar plot (Fig. 8‘a’) confirms this, where the red and

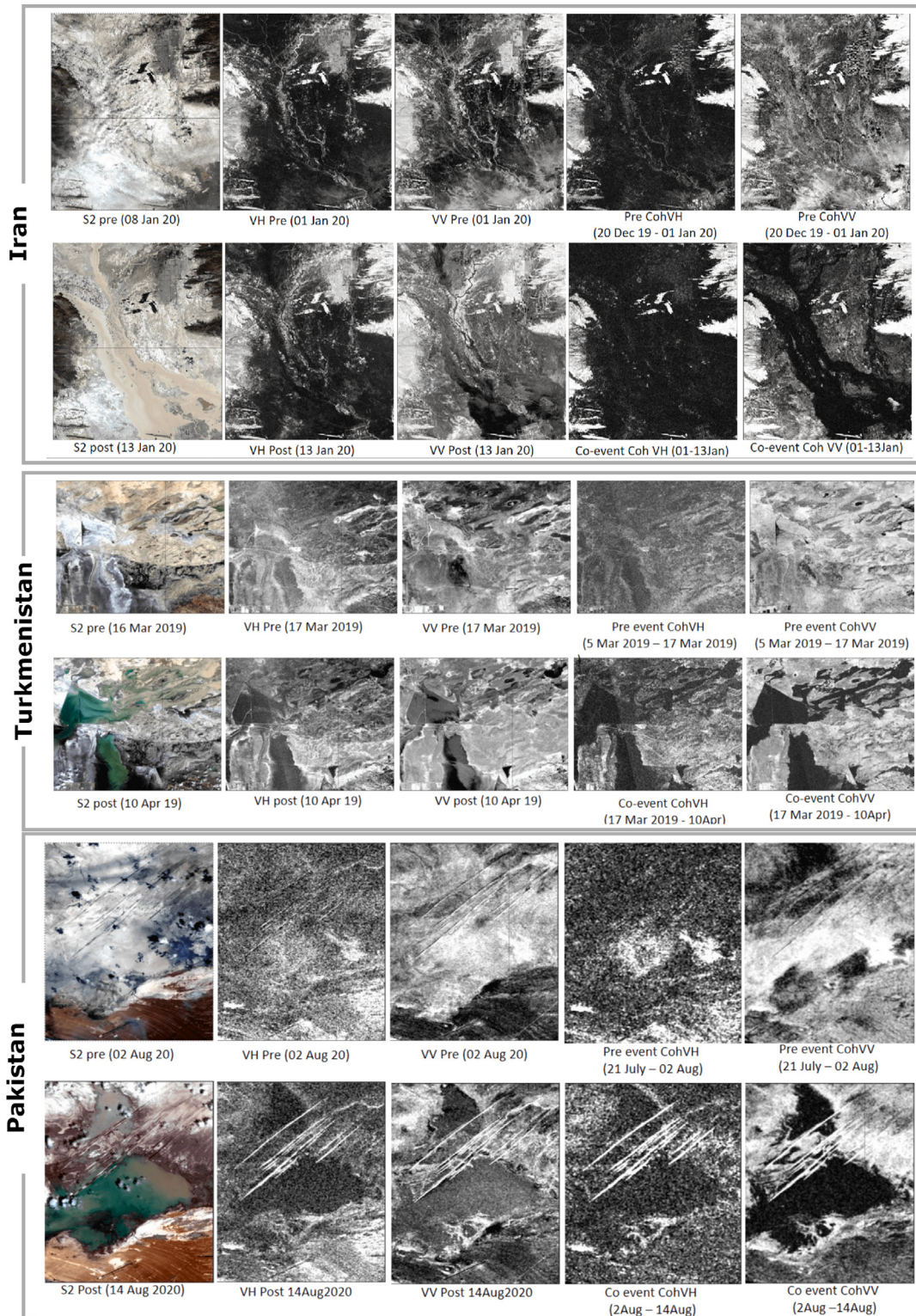


Fig. 4. The Figure shows data from Iran, Turkmenistan, and Pakistan. The first column in each case study shows Sentinel-2 (B4/B3/B2) images before and after floods to compare affected areas. The second and third columns display Sentinel-1 SAR data in VH and VV polarization before and during the flooding event. In the second row, the fourth and fifth columns present the co-flood coherence in VV and VH polarizations respectively. These coherence images demonstrate the temporal changes and phase correlations between the pre-flood and post-flood radar images. In the first row, the fourth and fifth columns showcase the pre-flood coherence in VH and VV polarizations respectively.

green lines show a reversal in the UA and PA values, such that Scenario 5 exhibits lower UA but higher PA than Scenario 4. In the case of Turkmenistan and Pakistan, all accuracy metrics show substantial improvements in arid flood detection accuracy when using coherence

compared to amplitude information, as seen in the radar charts ‘b’ and ‘c’ of Fig. 8. However, visually, in Turkmenistan, despite overall visual improvements, the emergence of new over-predicted areas is also noticeable, particularly near the flood boundaries (increased red

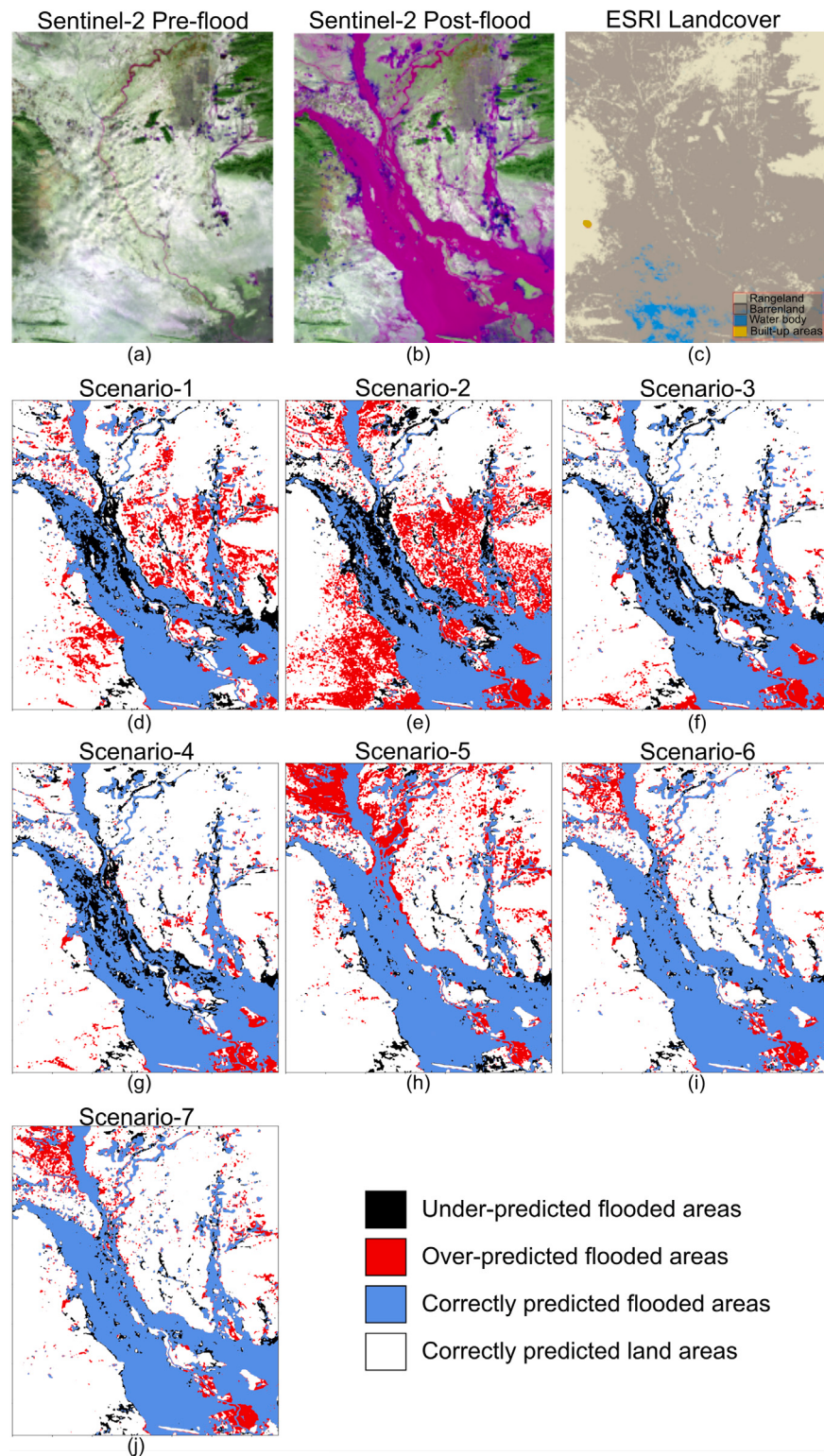


Fig. 5. Experimental results for Iran: (a) pre-flood and (b) post-flood Sentinel 2 in false-color composite (B8, B11, B2); ESRI 2019 Landcover is represented in (c). Subplots (d–j) display the contingency maps for Scenarios 1–7, employing color-coding to signify different predictions: overestimated areas in red, underestimated areas in black, correctly mapped flood regions in blue, and accurately delineated non-flooded areas in white. (For interpretation of the references to color in this figure legend, the reader is referred to the web version of this article.)

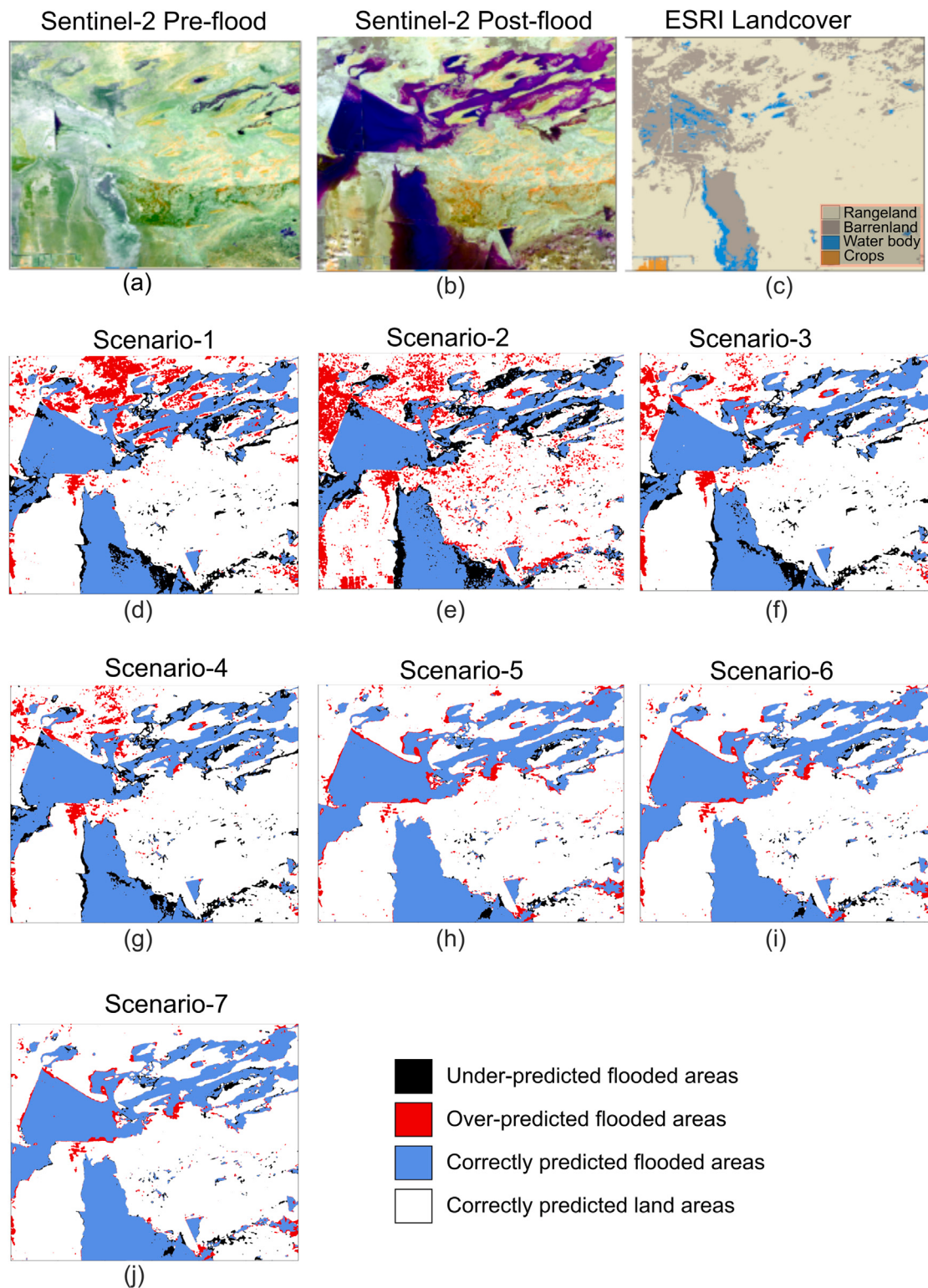


Fig. 6. As for Fig. 5 except for Turkmenistan case-study: (a) pre-flood and (b) post-flood Sentinel 2 in false-color composite (B8, B11, B2); ESRI 2019 Landcover is represented in (c). Subplots (d–j) display the contingency maps for Scenarios 1–7. (For interpretation of the references to color in this figure legend, the reader is referred to the web version of this article.)

regions near the flood boundaries in Figs. 6 'g' and 'h'). Pakistan mirrors this pattern, as over-predictions can be seen in the bottom right of the coherence-based flood masks (Scenario 5), which were absent in amplitude (Scenario 4) (Figs. 7 'g' and 'h').

When combining both amplitude and co-flood coherence in Scenario 6, Fig. 5'i shows a notable reduction in over-predictions in the top left of the panel as compared to Scenario 5 (Fig. 5'h) for Iran. Additionally, there is a noticeable improvement along the flood boundaries when compared with Scenario 5. Similarly, in Pakistan (5'h, and 'i'), a notable reduction in over-predictions can be observed in the bottom half of the image.

Fusing coherence with amplitude (Scenario 6) data yields higher metric scores across the board. IOU scores see increases of 12%, 21%, and 26%, while F1 scores improve by 5%, 11%, and 11% for Iran, Turkmenistan, and Pakistan, respectively, when compared to amplitude-only scenarios (Scenario 4). In the radar plot (Fig. 8a–c), the accuracy metrics clearly show that the fusion of amplitude and coherence (Scenario 6) surpasses both amplitude-only (Scenario 4) and coherence-only (Scenario 5) approaches for all three case studies (the blue line is noticeably higher than the red and green lines in nearly all the accuracy metrics).

4.3. Impact of pre-flood information

Scenario 1, using only post-flood amplitude images in VV and VH polarizations, depicts much overestimation (red regions) and underestimation (black regions) of flood areas across all case studies. In contrast, Scenario 4, which employs CD with pre-flood and post-flood images in both polarizations, substantially reduces these misclassifications (compare panel 'd' and 'g' in Figs. 5, 6, and 7). Quantitatively, adding pre-flood information notably enhances mapping accuracy, with IOU improvements of 21%, 13%, and 24% and F1 scores by 14%, 8%, and 15% in the case of Iran, Turkmenistan, and Pakistan respectively. This is evident from the radar plots (the red line is always higher than magenta in all the cases in Fig. 8a–c).

To understand if adding pre-flood coherence information improves flood detection, we designed and tested Scenario 7. The addition of the pre-flood coherence illustrates visually indiscernible changes from Scenario 6 in all cases studies (subplots 'i' and 'j' in Figs. 5, 6, 7). Quantitatively, only a marginal 1% increase in IOU was noted for Turkmenistan, with no further improvements observed in Iran and Pakistan. The radar plots (Fig. 8) display an overlap between Scenarios 6 and 7 for Iran and Pakistan (superimposing Scenario 6 and Scenario 7 lines in the case studies) suggesting that the addition of pre-flood coherence does not substantially enhance the model's performance.

4.4. Quantifying feature importance for arid flood detectability

In addition to gaining insights into the effects of various features on arid flood mapping across the different scenarios, we employed PFI to quantify the individual contributions of specific features to the model's predictive power. Fig. 9 presents the relative importance of each feature used in our predictive model in the first column, represented by the mean decrease in prediction IOU or model accuracy when the particular feature is "shuffled". The corresponding Pearson's correlation matrix, presented in the second column, assists in interpreting feature importance. This is particularly relevant, as the correlated features can compensate for each other, thereby reducing the observed importance of all the correlated features (Altmann et al., 2010).

In all case studies, 'Coh VV' emerged as the most important feature for flood detection in arid areas. Permuting 'Coh VV' would result in notable mean accuracy decreases of 16%, 20%, and 28% in the case of Iran, Turkmenistan, and Pakistan, respectively (Fig. 9a, c, e). Looking at the correlation plots of Turkmenistan and Pakistan (Fig. 9d,f) 'Coh VV' does not have a high correlation with any other features suggesting that it is indeed providing unique information crucial for the model's

Table 5

Accuracy metric comparison — All layer stack ('All') versus the optimum best three layer stack ('Opt') for Iran, Turkmenistan ('Turk'), and Pakistan ('Pak').

		OA	UA	PA	IOU	F1
Iran	All	0.91	0.87	0.86	0.76	0.87
	Opt	0.90	0.88	0.84	0.75	0.86
Turk	All	0.95	0.93	0.92	0.86	0.93
	Opt	0.95	0.93	0.92	0.86	0.92
Pak	All	0.95	0.92	0.91	0.85	0.92
	Opt	0.95	0.94	0.90	0.85	0.92

predictions. For Iran, 'Coh VV' shows a high correlation with 'Coh VH' (0.8) (Fig. 9b), which may explain the low feature importance of 'Coh VH' in all cases. However, the importance of coherence for the detection of arid floods in the region is undoubtedly clear in the three case studies.

Following 'Coh VV', 'VV Pre' and 'VV Post' emerge as the next common input features important across all cases. The permutation of 'VV Post' results in a 11% accuracy drop in Iran and 3% in Turkmenistan, while 'VV Pre' affects accuracy by 6%, 2%, and 9% in Iran, Turkmenistan, and Pakistan respectively (Fig. 9a, c, e). Our scenario analysis also supports these findings, showing that changes in VV polarization, involving both 'VV pre-flood' and 'VV post-flood', improve accuracy.

4.5. Optimizing flood detection - Precision vs. Complexity

In our analysis of the three case studies, the Coh VV, VV Post, and VV pre-flood stood out for their significant impact. To explore the impact of using a smaller feature set, which will not only reduce training and prediction time, but also improve interpretability, we trained an RF model with just these key features. Our goal was to assess the balance between maintaining model accuracy and improving time efficiency and interpretability. Fig. 10 contrasts the predictions made using the complete set of eight features against those made with the three most critical features. The differences are subtle but noticeable, such as the slight over-prediction in specific areas of Iran and Pakistan with the three-feature model that is not visible with the full feature set.

Table 5 summarizes the accuracy metrics for both the full feature set ('All') and the three-feature set ('Opt') across the studies. The results show only slight variations. For example, in Iran, switching to the three-feature set reduced the IOU and F1 scores by 1% each. In Turkmenistan, the F1 score dropped by 1%, while in Pakistan, the PA slightly increased by 1%, and the UA decreased by 2%, with other metrics staying consistent. Despite these minor changes in accuracy, the reduced feature set, chosen based on PFI analysis, performed comparably to the full set, considerably reducing computation times.

5. Discussion

5.1. Impact of SAR polarization

The results of our study show that CD using VV polarized (Scenario 3) performs noticeably better than VH polarized data (Scenario 2) for arid flood detection (panels 'e' and 'f' in Figs. 5, 6, and 7). A comparison of VH and VV images (second and third columns in Fig. 4) reveals that the VH polarization consistently exhibits low backscatter in all case studies. This is attributed to the fact that VH polarization is more sensitive to volume scattering (Earthdata, 2019), which typically occurs in vegetation. In barren, dry sandy areas with smooth surfaces and lacking vegetation, radar waves with VH polarization are likely to penetrate sandy soils, resulting in low backscatter values resulting mainly from subsurface volume scattering (Wagner et al., 2022). This is because cross-polarizations are relatively less sensitive to surface roughness (Wu et al., 2019), making them less effective for detecting

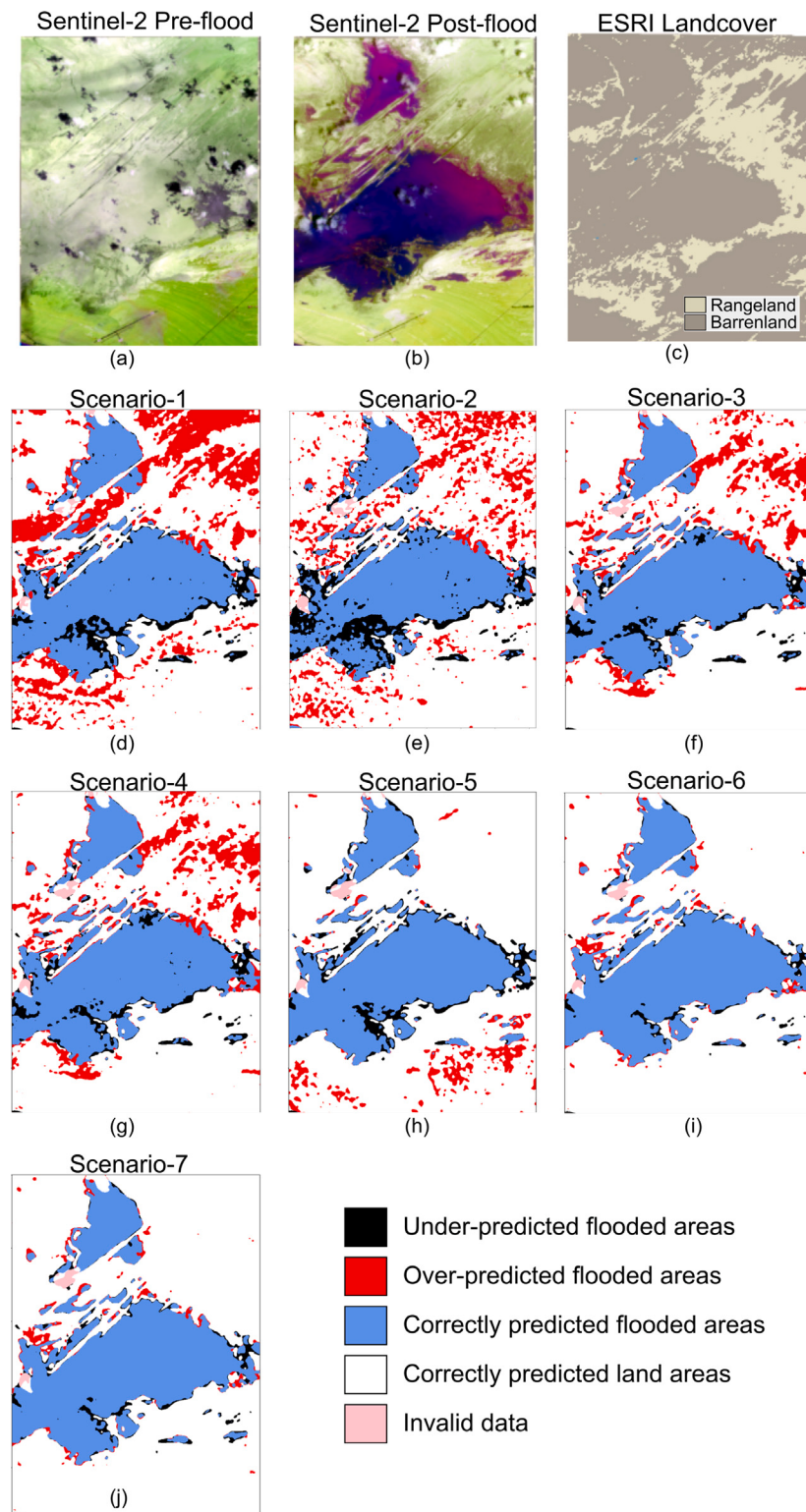


Fig. 7. As for Fig. 5 except for Pakistan case-study: (a) pre-flood and (b) post-flood Sentinel 2 in false-color composite (B8, B11, B2); ESRI 2019 Landcover is represented in (c). Subplots (d–j) display the contingency maps for Scenarios 1–7. (For interpretation of the references to color in this figure legend, the reader is referred to the web version of this article.)

backscatter from dry sandy surfaces. In contrast, VV provides relatively higher backscatter responses in dry areas. Incorporating VH information did not majorly improve OA, but did slightly enhance accuracy metrics, suggesting certain areas benefit from VH polarization. Future research should investigate regions more responsive to VH polarization and explore the underlying factors.

5.2. Impact of fusing amplitude and coherence

While both amplitude and coherence individually have merits as well as uncertainties, their fusion noticeably reduces misclassifications, improving flood mapping accuracy in arid regions. The primary challenge of using only amplitude data is the potential confusion with

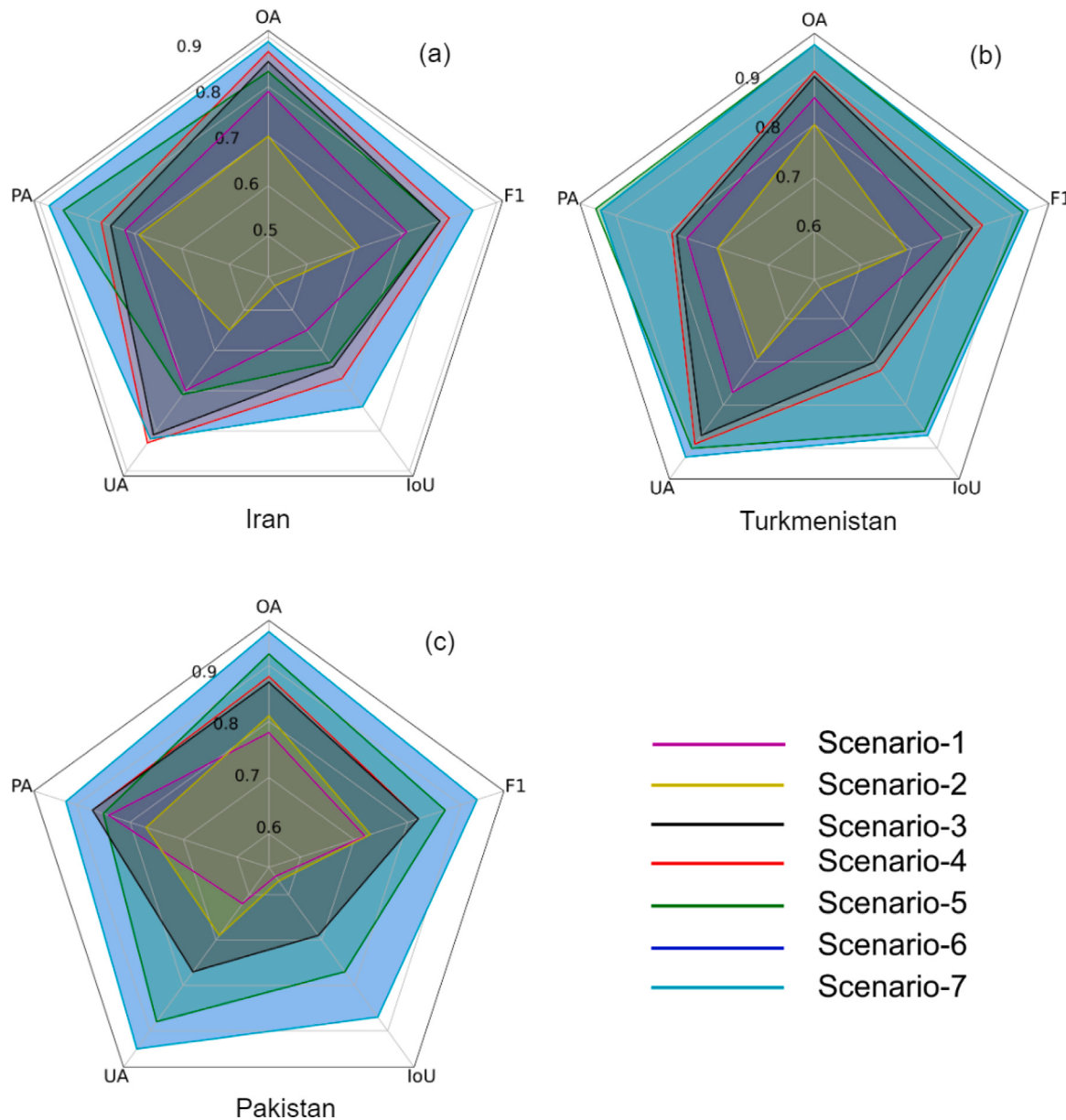


Fig. 8. Spyder plots: Accuracy assessment plots corresponding to three case studies. Each corner of the plot symbolizes a different accuracy metric, while the seven individual lines within the plot signify the performance across the seven different scenarios tested. It is notable that the lines for Scenario 6 (blue) and Scenario 7 (cyan) are mostly the same and overlap for all the metrics across the case studies. (For interpretation of the references to color in this figure legend, the reader is referred to the web version of this article.)

dry sandy surfaces, since water and dry sand exhibit similar backscatter (Martinis et al., 2018). Coherence information alone can also be misleading as changes in vegetation (for example, deforestation or harvesting) or man-made structures between image acquisitions could cause a drop in coherence (Villarroya-Carpio et al., 2022), leading to false flood detection.

The fusion of amplitude and coherence presents a practical solution to the challenges identified in each dataset above. While amplitude is influenced by surface characteristics related to the dielectric constant (indicative of soil moisture) and surface roughness, coherence quantifies the geometric similarity between two complex SAR images, reflecting the temporal stability of the surface observed between the images (Touzi et al., 1999). Low amplitude in arid regions is mainly due to a combination of low dielectric constant (Wagner et al., 2022; Mirsoleimani et al., 2019) and surface roughness (Hein, 2004). Coherence, however, also accounts for phase correlation between the waves during the two acquisitions, and therefore may not always result in low values in arid regions. Given no changes in the area under observation, a SAR

satellite observing it with identical sensor geometry on two separate occasions should produce the same phase angle of return, i.e. the returned waves would be coherent with one another. Flooding events alter surface characteristics, thereby reducing the coherence (Chini et al., 2019). Flooded sandy areas would show not only low amplitude, but also low coherence.

In contrast, non-flooded sandy areas, while having a low amplitude, would not show a drastic change and hence maintain relatively high coherence. The Copernicus Sentinel-1 constellation is ideal for such a study, as predictable and exact orbits with minimal displacements are ideal for coherence studies (refer to Sections 1.3 and 2.1). While improvements in algorithms have minimized coherence decorrelation due to system and processing factors, temporal decorrelation in dry arid regions could result from various anthropogenic activities in addition to flooding, including aeolian erosion, vehicle tracks, and moving vegetation (Schepanski et al., 2012; Chen et al., 2021; Preiss and Stacy, 2006). However, our analysis for the study period showed no evidence of significant sand movements that would indicate aeolian erosion.

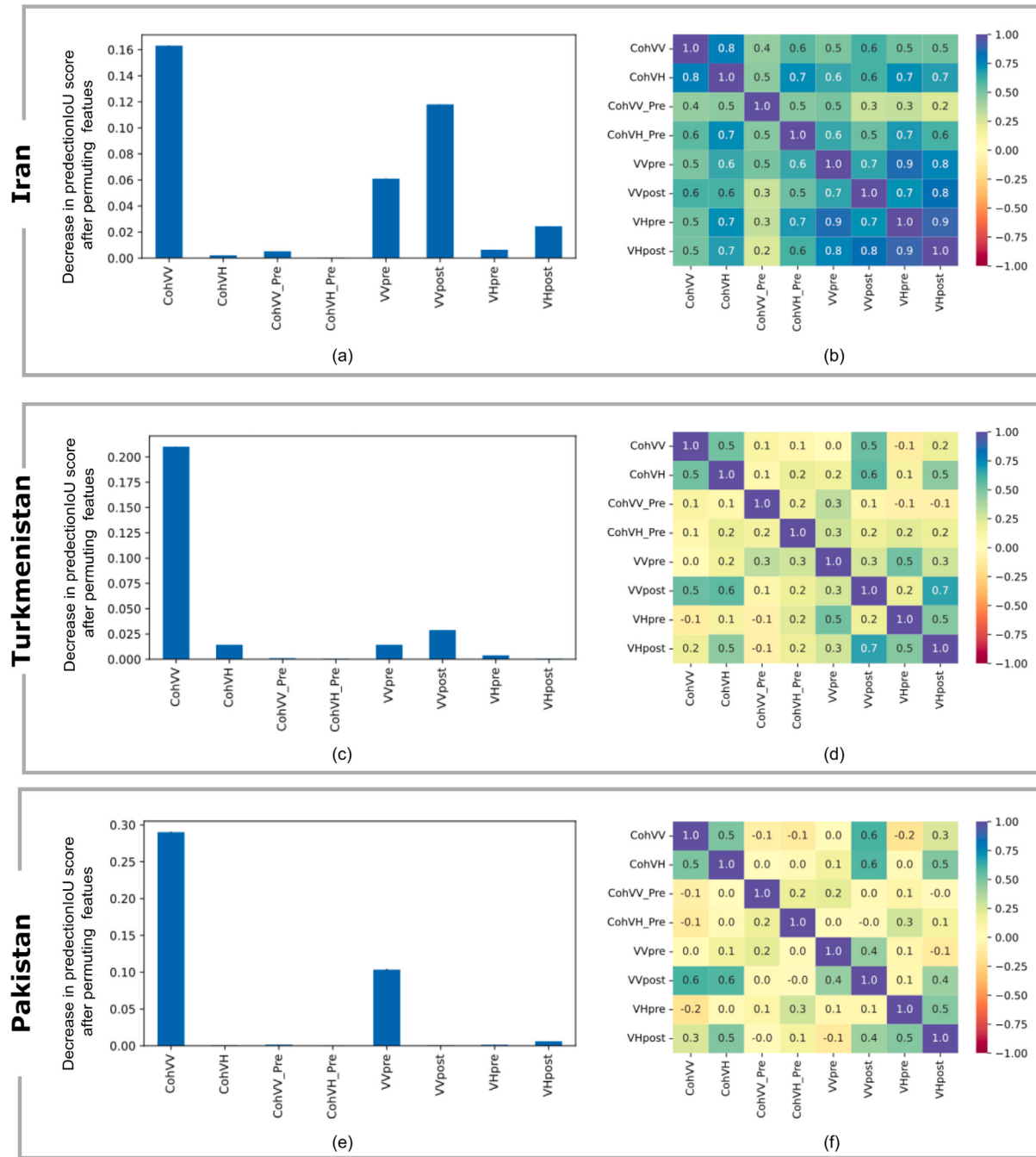


Fig. 9. The first column displays plots of mean decrease in IoU for each of the eight features on the x-axis, indicating their feature importance in arid region flood detection. A larger decrease in accuracy emphasizes the crucial role of that particular feature in the model's performance. The second column displays feature correlation heatmaps, showing the Pearson correlation among the different features in each colored cell. Rows represent different case studies. (For interpretation of the references to color in this figure legend, the reader is referred to the web version of this article.)

Vehicle tracks and signs of human activity in arid environments, which typically appear as straight, artificial lines in coherence images (Schepanski et al., 2012), were not identified across our study area. Given the aridity of our study region, the impact of vegetation on coherence is expected to be minimal. No noticeable vegetation was visible in Sentinel-2 imagery of the area. While sparse vegetation might exist and potentially affect coherence, its impact was considered negligible for this study. Moreover, our use of pre-flood coherence should account for any minor vegetation-related effects. While there is currently limited research on arid flood mapping to provide direct support for our findings, our study aligns with previous work that combines amplitude

data with coherence from other SAR sensors such as ERS, TerraSAR-X, and COSMO-SkyMED data to improve flood mapping in vegetated and urban areas where amplitude data alone is insufficient to detect flooding (Refice et al., 2014; Nico et al., 2000; Li et al., 2019).

5.3. Impact of including pre-flood information

The study results show that amplitude CD (Scenario 4) reduces misclassification compared to post-flood amplitude data (Scenario 1). The improved accuracy in amplitude CD than using just the post-flood is because sandy surfaces generally maintain relatively consistent

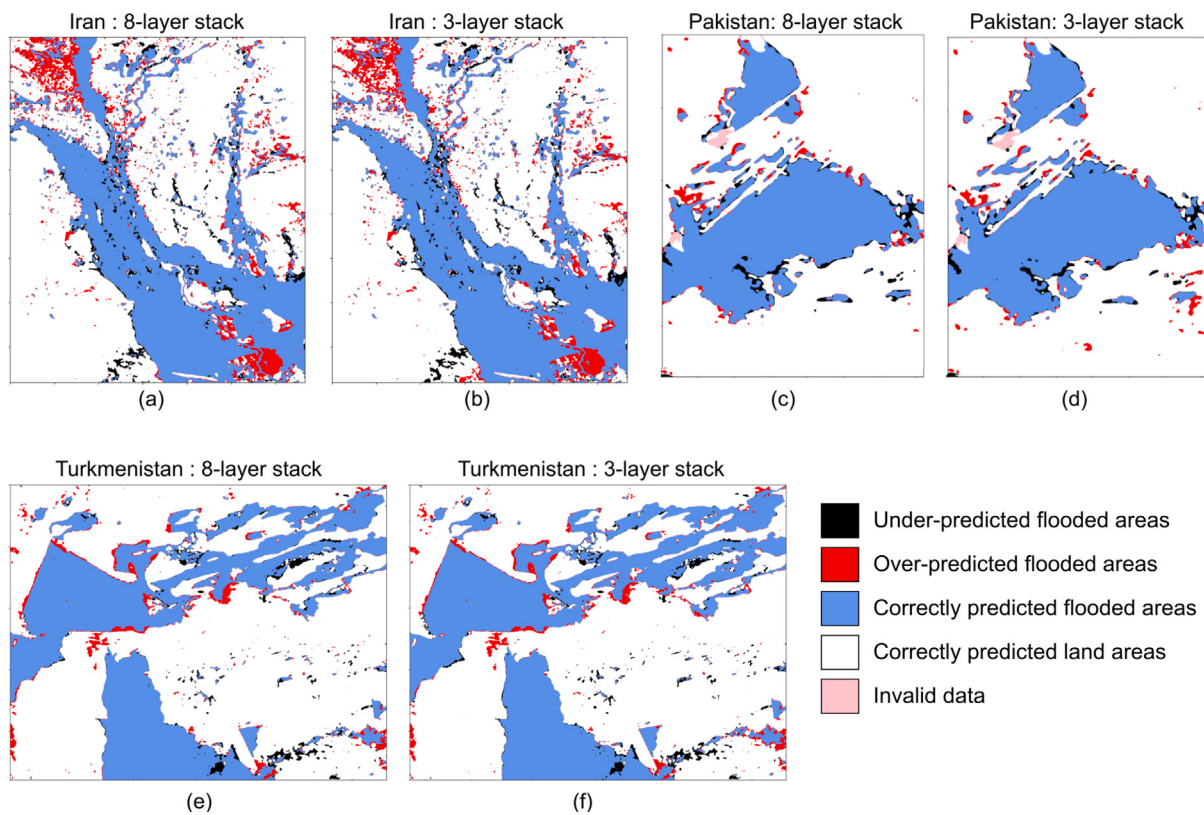


Fig. 10. Accuracy map derived from the model trained using all eight features versus accuracy map obtained from the model considering the three best features – co-flood coherence, pre-flood and flooded amplitude – all in VV polarization.

backscatter, whereas flooded areas tend to display a change in backscatter when comparing pre-flood and post-flood imagery. This aligns with previous studies where CD techniques were successfully applied to flood mapping in other land cover classes (Vanama et al., 2021a; Clement et al., 2018).

Vanama et al. (2021a) and Clement et al. (2018). The integration of temporal data through CD thus emerges as a powerful tool for enhancing flood detection accuracy, particularly in complex terrain.

For coherence, we found that only co-flood coherence notably improved flood detection accuracy, while the addition of pre-flood coherence information provided minimal benefits. This finding can be attributed to the nature of coherence as it is a change metric (Touzi et al., 1999). Co-flood coherence inherently captures the changes occurring during the flood event, making it particularly effective for identifying flood-affected areas. In contrast, pre-flood coherence, representing conditions before the event, did not contribute substantial additional information for flood detection in our study areas. Nevertheless, in certain circumstances, such as areas with typically low coherence, using pre-flood coherence information could enhance the accuracy of the flood mapping model. These regions might exhibit low coherence due to a variety of factors such as dense vegetation, viewing geometry, topographic effects, permanent water bodies, or urban zones with high human activity, all manifesting temporal changes (Olen and Bookhagen, 2020; Villarroya-Carpio et al., 2022). Recognizing these regions using pre-flood coherence data allows separate processing during flood detection, mitigating potential overestimations by examining the low coherent values (Budkevitsch et al., 2000). While our study did not specifically focus on the influence of permanently low coherence areas, their impact on flood mapping accuracy highlights an important area for continued investigation.

5.4. Optimizing the machine learning model

In considering time constraints, we investigated the role of different features in predicting the flood map. For the Iran dataset, a

full deployment with all eight features resulted in 8000 training data points, as opposed to a smaller 3000 points with the top three features. The practical implications of this selection are evident when assessing the model's training time: in the Iran case, the all-feature setup took 884 ms, whereas narrowing down to the best features reduced this to 544 ms, approximately 35% less time. When working with complex deep learning models or scaling globally to near-real-time solutions, 35% time savings could mean data-driven or blind decision-making, especially in flood emergencies. We used nVidia Quadro P4000 (GP104GL) with 512 GB memory. The machine had 2 Intel (R) Xeon (R) Gold 5222 CPU @ 3.80 GHz (each 4 cores/8 threads). In terms of performance accuracy, the transition from the all-feature model to the top three features revealed only a marginal drop in performance metrics. This suggests that we can achieve nearly comparable accuracy in a fraction of the time with an optimum feature set. A model built on fewer features offers enhanced explainability (Hastie et al., 2009b). Such models are more transparent and simpler to interpret, which can be advantageous in cases where we need rapid flood mapping and a better understanding of the model's decision-making process (Gosiewska et al., 2021).

In addition to optimizing feature selection, we also examined the feasibility of using pre-trained models for flood detection in operational contexts. Using the optimal model with VV amplitude (pre-flood and post-flood) and VV co-flood coherence we tested its performance across different regions. When the model trained on Iran data was tested on Turkmenistan and Pakistan, there was a performance drop of 23% and 36% in IOU and 36% and 24% in F1 respectively (see Fig. 11). Performance drop indicates reduced effectiveness (when there is less generalizability in training data). However, training models on combined datasets (Iran-Turkmenistan tested on Pakistan, and Iran-Pakistan tested on Turkmenistan) improved performance compared to single-region models by almost 50% for Pakistan and 75% for Turkmenistan. The improved model performance suggests that training

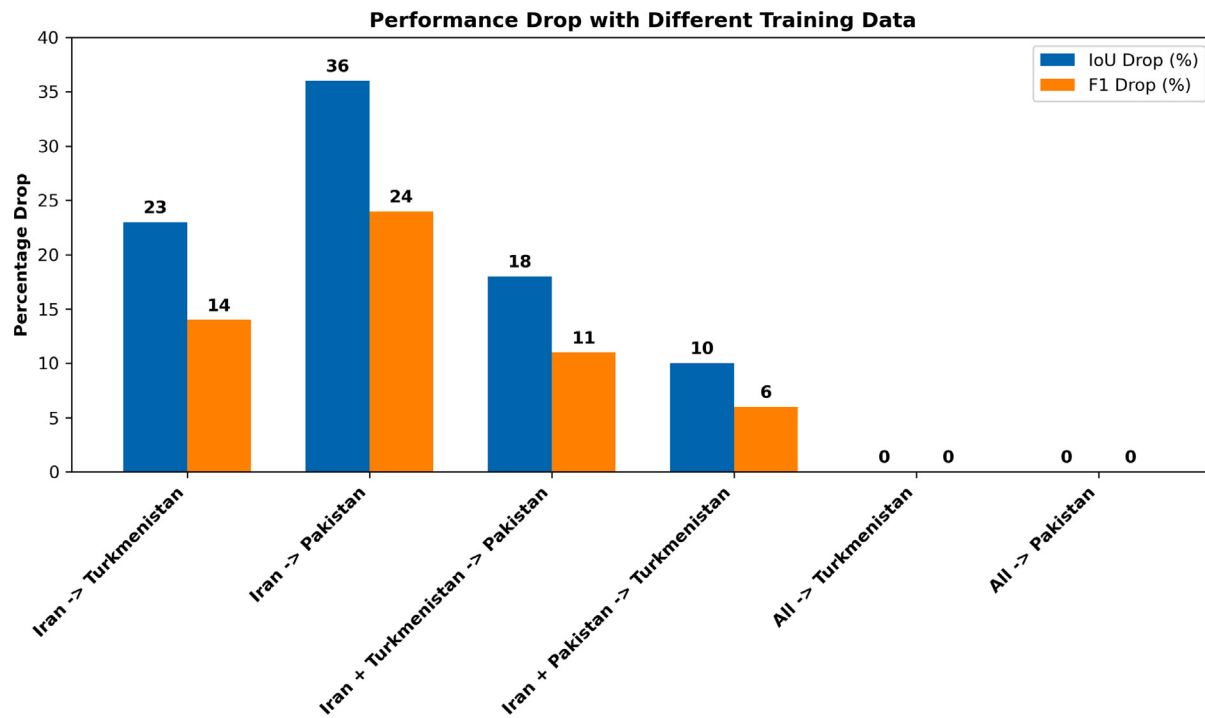


Fig. 11. The Figure illustrates the performance drop, measured in terms of IOU and F1 score when using pre-trained flood detection models across different regions. Specifically, the optimal model, trained with VV amplitude (pre-flood and post-flood) and VV co-flood coherence data, was trained and tested on various combinations of regions. The x-axis labels follow the format 'Training Data -> Testing Data', where the data before the arrow indicates the training dataset and the data after the arrow indicates the testing dataset.

with diverse data enhances the generalizability of the flood detection model. Furthermore, a model trained on data from the three regions achieved IOU and F1 scores comparable to those of region-specific models, demonstrating effective generalization in different areas. While the purpose of this study was not to evaluate the performance of different models, the results highlight the potential of using pre-trained models for flood detection in operational contexts. These results are particularly encouraging, showing potential even with a simple RF model and just three case studies. Our findings suggest that with more case studies and advanced deep learning methods capable of learning deeper features (Ghosh et al., 2024), the performance and generalizability of the model could be further improved for operational use.

5.5. Challenges and opportunities for operational arid flood mapping

The performance of the flood detection RF model presented herein can be attributed to the task-specific model training for flood detection. However, when flooding is absent, the model can overpredict in an operational context. The feature importance plots (Fig. 9) and feature histograms (refer to Fig. A.4) show the model relies on low coherence values. While low coherence in this study is attributable to flooding, other factors such as vegetation, construction activities, and other events can also cause a decrease in coherence, potentially leading to misclassifications (Abdel-Hamid et al., 2021; Chen et al., 2021; Haiqin et al., 2013). However, this challenge is not unique to coherence; current flood detection methods based on amplitude CD and time series also generate change maps, and attributing the change remains a problematic task (DeVries et al., 2020). Future work should develop methods to separate flood-related signals among others, which is critical from an operational standpoint, where differentiating flood-related signals from other causes is essential.

Another crucial aspect in operational flood mapping is the acquisition of additional features since it is currently the most time-intensive process as computational resources expand. The inclusion of coherence, for instance, necessitates the selection of pre-flood data in a

specific configuration involving spatial and temporal baseline combinations. Optimal coherence requires minimizing both spatial and temporal baselines to reduce geometric and temporal decorrelation, respectively (Ferretti et al., 2007). It is critical that the pre-flood image is not acquired during a rainfall event, as the SAR backscatter is attenuated through rain depending on rain rate (Doblas et al., 2020). If the rains are heavy, attenuation can cause artifacts which could potentially lead to a misinterpretation of flood extent (Danklmayer and Chandra, 2009). Any temporary or seasonal water bodies present in pre-flood imagery should also be carefully documented to differentiate them from actual flood waters. The quality of coherence data will further influence flood mapping results, making its integration with current methods complex and non-trivial.

Given these considerations, it is crucial to investigate criteria for using coherence data in flood mapping. The effectiveness of coherence data depends on the context: when amplitude data is insufficient and coherence offers an advantage, it is warranted. The results of this study demonstrate notable improvements in flood mapping by including coherence with amplitude information in arid regions. Previous studies have corroborated the value of coherence in urban flood mapping (Zhao et al., 2022; Chini et al., 2019). To optimize coherence use, further experiments that analyze a diverse range of case studies are necessary. For instance, areas with consistently high coherence (e.g., bare soil and rock outcrops) might be more reliable for detecting subtle changes due to flooding, while areas with naturally low coherence might require additional information.

By identifying conditions in which coherence data improve flood mapping accuracy, more targeted and efficient flood mapping strategies can be developed, along with criteria for best leveraging coherence data. Advancements in cloud computing and platforms such as ASF and Amazon Web Services (AWS) have made coherence calculation more accessible (Kellndorfer et al., 2022; Global). Recent work by Zhao et al. (2024) on an urban flood data set that incorporates coherence data is a promising step forward. Such datasets including interferometric coherence provide valuable opportunities to test and refine models, reducing the scalability issues related to coherence calculations

and helping establish best practices for leveraging coherence data to determine where it may and may not be applicable. Based on our findings that VH polarization is less effective for flood mapping in arid environments, future research should explore the impact of factors like spatial, and temporal baselines, wavelength, incidence angle, and effect of land cover on backscattering and coherence for flood mapping accuracy (Preiss and Stacy, 2006; Hein, 2004; Amitrano et al., 2024). Importantly, studies should also document cases where algorithms fail, as understanding these limitations is key to improving our understanding of algorithmic shortcomings and refining existing methods for more robust, globally applicable flood mapping solutions.

6. Conclusion and outlook

In this paper, we present a detailed investigation of the use of different layers of SAR information to improve arid flood mapping, an area that has remained under-researched due to the challenges in differentiating between dry sand and water in SAR imagery. Our approach enhances understanding and accuracy by integrating amplitude and coherence data from bi-temporal SAR, which was tested on three distinct real flood events in dry regions of Iran, Turkmenistan, and Pakistan.

Focusing on SAR amplitude data, used commonly in flood mapping, our study reveals two important findings. Firstly, the inclusion of pre-flood imagery with post-flood imagery markedly improves flood mapping accuracy over using only post-flood imagery. This enhancement was clear in our results, showing approximately a 25% increase in IOU and a 16% rise in F1 scores. Secondly, in terms of polarization, amplitude data in VV polarization was consistently more effective than VH polarization for flood detection in arid regions, with an average increase of 29% in IOU and 12% in F1 scores across our case studies. A critical outcome of our research is that combining coherence and amplitude information considerably improves arid flood mapping, outperforming methods that rely solely on either coherence or amplitude. Integrating coherence and amplitude demonstrated major improvement in all scenarios tested, with the IOU and F1 scores increasing by around 20% and 10%, respectively. While the inclusion of pre-flood coherence data offered some benefits, it did not greatly impact the overall results.

Our feature importance analysis identified three critical features for accurate flood mapping in arid regions: amplitude CD in VV polarization, and co-flood coherence in VV polarization. The results demonstrate that models trained with these selected features closely matched the accuracies of models using all layers of information, while notably reducing processing times, which is crucial for rapid response in disaster scenarios, allowing for quicker and equally accurate flood mapping with better explainability and reduced computational demands. In addition, our study suggests that training flood detection models with diverse data enhances their generalization capacity, improving performance across different regions. This is particularly encouraging, showing potential even with simple models, and indicates that with more case studies and advanced methods, pre-trained models could become effective.

The study offers opportunities for improving global flood mapping. While we acknowledge integrating coherence data into the CEMS Global Flood Monitoring system presents challenges in terms of processing time, storage, and financial costs, the results of this study highlight its potential benefits in arid floods, with other studies showing promise for urban flooding. With the increasing availability of SLC data from SAR missions and advancements in cloud-based processing tools, coherence calculation is becoming more scalable and accessible. For instance, the ASF and AWS provide coherence calculation capabilities on the cloud. Future studies should leverage these developments to conduct more experiments across case studies, better understand the feasibility of merging amplitude and coherence data, and further develop criteria to fully harness the potential of SAR for flood mapping.

CRediT authorship contribution statement

Shagun Garg: Writing – review & editing, Writing – original draft, Visualization, Validation, Software, Resources, Project administration, Methodology, Investigation, Formal analysis, Data curation, Conceptualization. **Antara Dasgupta:** Writing – review & editing, Supervision, Conceptualization. **Mahdi Motagh:** Writing – review & editing, Supervision, Funding acquisition, Conceptualization. **Sandro Martinis:** Writing – review & editing, Supervision, Conceptualization. **Sivasakthy Selvakumaran:** Writing – review & editing, Supervision, Funding acquisition, Conceptualization.

Declaration of competing interest

The authors declare that they have no known competing financial interests or personal relationships that could have appeared to influence the work reported in this paper.

Data availability

All the data is publicly available and free to use.

Declaration of Generative AI and AI-assisted technologies in the writing process

During the preparation of this work, the authors used ChatGPT to improve language and readability. After using this tool, we reviewed and edited the content as needed and took full responsibility for the content of the publication.

Acknowledgments and funding information

The authors gratefully acknowledge the EPSRC and BP for funding this research through the EPSRC Centre for Doctoral Training in Future Infrastructure and Built Environment: Resilience in a Changing World (Grant number: EP/S02302X/1) and to the Helmholtz Artificial Intelligence Cooperation Unit, Germany for partial funding under the project “AI for Near Real-Time Satellite-based Flood Response” (AI4FLOOD), Helmholtz Information and Data Science Academy. Dr. Sivasakthy Selvakumaran was supported by the Isaac Newton Trust. Additionally, we acknowledge ESA Copernicus for granting access to the Sentinel-1 and Sentinel-2 datasets, which were instrumental in this research.

Appendix A. Supplementary data

Supplementary material related to this article can be found online at <https://doi.org/10.1016/j.rse.2024.114417>.

References

- Abdel-Hamid, Ayman, Dubovik, Olena, Greve, Klaus, 2021. The potential of sentinel-1 InSAR coherence for grasslands monitoring in Eastern Cape, South Africa. *Int. J. Appl. Earth Obs. Geoinf.* (ISSN: 1569-8432) 98, 102306. <http://dx.doi.org/10.1016/j.jag.2021.102306>, URL <https://www.sciencedirect.com/science/article/pii/S0303243421000131>.
- Adhikari, Ruma, Tsutsumida, Narumasa, Bhardwaj, Alok, 2023. An index-based flood mapping using Stokes parameters of multitemporal SAR images: 2019 hagibis flood event of Ibaraki, Japan. In: IGARSS 2023 - 2023 IEEE International Geoscience and Remote Sensing Symposium. pp. 7194–7197. <http://dx.doi.org/10.1109/IGARSS52108.2023.10281581>, URL <https://ieeexplore.ieee.org/document/10281581>.
- Albertini, Cinzia, Gioia, Andrea, Iacobellis, Vito, Petropoulos, George P., Manfreda, Salvatore, 2024. Assessing multi-source random forest classification and robustness of predictor variables in flooded areas mapping. *Remote Sens. Appl. Soc. Environ.* (ISSN: 2352-9385) 35, 101239. <http://dx.doi.org/10.1016/j.rse.2024.101239>, URL <https://www.sciencedirect.com/science/article/pii/S2352938524001034>.
- Altmann, André, Tolosi, Laura, Sander, Oliver, Lengauer, Thomas, 2010. Permutation importance: a corrected feature importance measure. *Bioinformatics* (ISSN: 1367-4803) 26 (10), 1340–1347. <http://dx.doi.org/10.1093/bioinformatics/btq134>, arXiv:https://academic.oup.com/bioinformatics/article-pdf/26/10/1340/48851160/bioinformatics_26_10_1340.pdf.

- Amitrano, Donato, Di Martino, Gerardo, Di Simone, Alessio, Imperatore, Pasquale, 2024. Flood detection with SAR: A review of techniques and datasets. *Remote Sens.* (ISSN: 2072-4292) 16 (4), <http://dx.doi.org/10.3390/rs16040656>, URL <https://www.mdpi.com/2072-4292/16/4/656>.
- Bauer-Marschallinger, Bernhard, Cao, Senmao, Navacchi, Claudio, Freeman, Vahid, Reuß, Felix, Geudtner, Dirk, Rommen, Björn, Vega, Francisco Ceba, Snoeij, Paul, Attema, Evert, Reimer, Christoph, Wagner, Wolfgang, 2021. The normalised sentinel-1 global backscatter model, mapping earth's land surface with C-band microwaves. *Sci. Data* 8, 277. <http://dx.doi.org/10.1038/s41597-021-01059-7>.
- Bauer-Marschallinger, Bernhard, Cao, Senmao, Tupas, Mark Edwin, Roth, Florian, Navacchi, Claudio, Melzer, Thomas, Freeman, Vahid, Wagner, Wolfgang, 2022. Satellite-based flood mapping through Bayesian inference from a sentinel-1 SAR datacube. *Remote Sens.* (ISSN: 2072-4292) 14 (15), URL <https://www.mdpi.com/2072-4292/14/15/3673>.
- Belgiu, Mariana, Drăgut, Lucian, 2016. Random forest in remote sensing: A review of applications and future directions. *ISPRS J. Photogramm. Remote Sens.* (ISSN: 0924-2716) 114, 24–31. <http://dx.doi.org/10.1016/j.isprsjprs.2016.01.011>, URL <https://www.sciencedirect.com/science/article/pii/S0924271616000265>.
- Bereczky, Max, Wieland, Marc, Krullikowski, Christian, Martinis, Sandro, Plank, Simon, 2022. Sentinel-1-based water and flood mapping: Benchmarking convolutional neural networks against an operational rule-based processing chain. *IEEE J. Sel. Top. Appl. Earth Obs. Remote Sens.* (ISSN: 2151-1535) 15, 2023–2036. <http://dx.doi.org/10.1109/JSTARS.2022.3152127>, URL <https://ieeexplore.ieee.org/document/9714780>.
- Bertram, A., Wendleder, A., Schmitt, A., Huber, M., 2016. Long-term monitoring of water dynamics in the sahel region using the multi-sar-system. *Int. Arch. Photogramm. Remote Sens. Spat. Inf. Sci.* XLI-B8, 313–320. <http://dx.doi.org/10.5194/isprs-archives-XLI-B8-313-2016>, URL <https://isprs-archives.copernicus.org/articles/XLI-B8/313/2016/>.
- Bevere, Lucia, Remondi, Federica, Aellen, Neil, Dhore, Kishor, Mussetti, Gianluca, Tuozzolo, Steve, 2023. Natural Catastrophes in 2021: the Floodgates are Open. Technical Report, Swiss Re Institute, Zurich, Switzerland, URL <https://www.swissre.com/institute/research/sigma-research/sigma-2022-01.html>.
- Bonafilia, Derrick, Tellman, Beth, Anderson, Tyler, Issenberg, Erica, 2020. Sen1Floods11: A georeferenced dataset to train and test deep learning flood algorithms for sentinel-1. In: Proceedings of the IEEE/CVF Conference on Computer Vision and Pattern Recognition (CVPR) Workshops. URL <https://ieeexplore.ieee.org/document/9150760>.
- Bovolo, Francesca, Bruzzone, Lorenzo, 2007. A split-based approach to unsupervised change detection in large-size multitemporal images: Application to tsunami-damage assessment. *IEEE Trans. Geosci. Remote Sens.* 45 (6), 1658–1670. <http://dx.doi.org/10.1109/TGRS.2007.895835>, URL <https://ieeexplore.ieee.org/document/4215033>.
- Breiman, Leo, Friedman, Jerome, Olshen, Richard A, Stone, Charles J, 1984. Classification and Regression Trees. Chapman and Hall/CRC, <http://dx.doi.org/10.1201/9781315139470>.
- Brisco, Brian, Ahern, Frank, Murnaghan, Kevin, White, Lori, Canisus, Francis, Lancaster, Philip, 2017. Seasonal change in wetland coherence as an aid to wetland monitoring. *Remote Sens.* (ISSN: 2072-4292) 9 (2), URL <https://www.mdpi.com/2072-4292/9/2/158>.
- Bukkewitsch, P., D'Iorio, M.A., Vachon, P.W., Pollard, W., Andersen, D.T., 2000. Geomorphologic, active layer and environmental changes detected in sar scene coherence images. In: Proceedings of the Sixth Circumpolar Symposium on Remote Sensing of Polar Environments. Yellowknife, NWT, p. 8, URL https://www.researchgate.net/publication/265033489_Sources_of_Phase_Decoration_in_SAR_Scene_Coherence_Images_from_Arctic_Environments. June 12–14.
- Canisius, Francis, Brisco, Brian, Murnaghan, Kevin, Van Der Kooij, Marco, Keizer, Edwin, 2019. SAR backscatter and InSAR coherence for monitoring wetland extent, flood pulse and vegetation: A study of the amazon lowland. *Remote Sens.* (ISSN: 2072-4292) 11 (6), URL <https://www.mdpi.com/2072-4292/11/6/720>.
- Cartus, Oliver, Santoro, Maurizio, Wegmüller, Urs, Labrière, Nicolas, Chave, Jérôme, 2022. Sentinel-1 coherence for mapping above-ground biomass in semiarid forest areas. *IEEE Geosci. Remote Sens. Lett.* 19, 1–5. <http://dx.doi.org/10.1109/LGRS.2021.3071949>, URL <https://ieeexplore.ieee.org/document/9410652/>.
- CEMS, 2023. Copernicus emergency management services. <https://emergency.copernicus.eu/>. (Accessed 06 October 2023).
- Charter, 2023. The international charter space and major disasters. <https://disasterscharter.org/>. (Accessed 06 October 2023).
- Chen, Yaogang, Sun, Qian, Hu, Jun, 2021. Quantitatively estimating of InSAR deformation based on landsat-derived NDVI. *Remote Sens.* (ISSN: 2072-4292) 13 (13), <http://dx.doi.org/10.3390/rs13132440>, URL <https://www.mdpi.com/2072-4292/13/13/2440>.
- Chini, Marco, Hostache, Renaud, Giustarini, Laura, Matgen, Patrick, 2017. A hierarchical split-based approach for parametric thresholding of sar images: Flood inundation as a test case. *IEEE Trans. Geosci. Remote Sens.* 55 (12), 6975–6988. <http://dx.doi.org/10.1109/TGRS.2017.2737664>, URL <https://ieeexplore.ieee.org/document/8017436>.
- Chini, Marco, Pelich, Ramona, Pulvirenti, Luca, Pierdicca, Nazzareno, Hostache, Renaud, Matgen, Patrick, 2019. Sentinel-1 InSAR coherence to detect floodwater in urban areas: Houston and hurricane harvey as a test case. *Remote Sens.* 11 (2), URL <https://www.mdpi.com/2072-4292/11/2/107>.
- Clement, M.A., Kilsby, C.G., Moore, P., 2018. Multi-temporal synthetic aperture radar flood mapping using change detection. *J. Flood Risk Manage.* 11 (2), 152–168. <http://dx.doi.org/10.1111/jfr3.12303>, URL <https://onlinelibrary.wiley.com/doi/abs/10.1111/jfr3.12303>. arXiv:<https://onlinelibrary.wiley.com/doi/pdf/10.1111/jfr3.12303>.
- Colditz, René Roland, 2015. An evaluation of different training sample allocation schemes for discrete and continuous land cover classification using decision tree-based algorithms. *Remote Sens.* (ISSN: 2072-4292) 7 (8), 9655–9681. <http://dx.doi.org/10.3390/rs70809655>, URL <https://www.mdpi.com/2072-4292/7/8/9655>.
- Danklmayer, Andreas, Chandra, Madhukar, 2009. Precipitation induced signatures in SAR images. In: 2009 3rd European Conference on Antennas and Propagation. pp. 3433–3437. <http://dx.doi.org/10.34385/proc.35.4A10-4>.
- Dasgupta, Antara, Grimaldi, Stefania, Ramsankaran, R.A.A.J., Pauwels, Valentijn R.N., Walker, Jeffrey P., 2018b. Towards operational SAR-based flood mapping using neuro-fuzzy texture-based approaches. *Remote Sens. Environ.* (ISSN: 0034-4257) 215, 313–329. <http://dx.doi.org/10.1016/j.rse.2018.06.019>, URL <https://www.sciencedirect.com/science/article/pii/S0034425718302979>.
- Dasgupta, Antara, Grimaldi, Stefania, Ramsankaran, RAAJ, Pauwels, Valentijn R.N., Walker, Jeffrey P., Chini, Marco, Hostache, Renaud, Matgen, Patrick, 2018a. Flood mapping using synthetic aperture radar sensors from local to global scales. In: Global Flood Hazard. American Geophysical Union (AGU), ISBN: 9781119217886, pp. 55–77. <http://dx.doi.org/10.1002/9781119217886.ch4>, (Chapter 4). URL <https://agupubs.onlinelibrary.wiley.com/doi/abs/10.1002/9781119217886.ch4>. arXiv:<https://agupubs.onlinelibrary.wiley.com/doi/pdf/10.1002/9781119217886.ch4>.
- DeLancey, Evan R., Brisco, Brian, Canisius, Francis, Murnaghan, Kevin, Beaudette, Liam, Kariyeva, Jahan, 2019. The synergistic use of RADARSAT-2 ascending and descending images to improve surface water detection accuracy in Alberta, Canada. *Can. J. Remote Sens.* 45 (6), 759–769. <http://dx.doi.org/10.1080/07038992.2019.1691516>, arXiv:<https://doi.org/10.1080/07038992.2019.1691516>.
- Delgado Blasco, José Manuel, Fitzyk, Magdalena, Patruno, Jolanda, Ruiz-Armenteros, Antonio Miguel, Marconcini, Mattia, 2020. Effects on the double bounce detection in urban areas based on sar polarimetric characteristics. *Remote Sens.* (ISSN: 2072-4292) 12 (7), URL <https://www.mdpi.com/2072-4292/12/7/1187>.
- Deng, Chengbin, Wu, Changshan, 2013. The use of single-date MODIS imagery for estimating large-scale urban impervious surface fraction with spectral mixture analysis and machine learning techniques. *ISPRS J. Photogramm. Remote Sens.* (ISSN: 0924-2716) 86, 100–110. <http://dx.doi.org/10.1016/j.isprsjprs.2013.09.010>, URL <https://www.sciencedirect.com/science/article/pii/S0924271613002116>.
- DeVries, Ben, Huang, Chengquan, Armston, John, Huang, Wenli, Jones, John W., Lang, Megan W., 2020. Rapid and robust monitoring of flood events using sentinel-1 and landsat data on the google earth engine. *Remote Sens. Environ.* (ISSN: 0034-4257) 240, 111664. <http://dx.doi.org/10.1016/j.rse.2020.111664>, URL <https://www.sciencedirect.com/science/article/pii/S003442572030033X>.
- Doblas, J., Carneiro, A., Shimabukuro, Y., Sant'Anna, S., Aragão, L., 2020. Assessment of rainfall influence on sentinel-1 time series on amazonian tropical forests aiming deforestation detection improvement. In: 2020 IEEE Latin American GRSS & ISPRS Remote Sensing Conference. LAGIRS, pp. 397–402. <http://dx.doi.org/10.1109/LAGIRS48042.2020.9165566>.
- Earthdata, NASA, 2019. What is synthetic aperture radar? <https://www.earthdata.nasa.gov/learn/backgrounder/what-is-sar#>. (Accessed 28 October 2023).
- Eslamian, S., Eslamian, F.A., 2022. Flood Handbook: Principles and Applications, first ed. CRC Press, <http://dx.doi.org/10.1201/9781003262640>.
- Fatras, C., Frappart, F., Mougin, E., Grippa, M., Hiernaux, P., 2012. Estimating surface soil moisture over sahel using ENVISAT radar altimetry. *Remote Sens. Environ.* (ISSN: 0034-4257) 123, 496–507. <http://dx.doi.org/10.1016/j.rse.2012.04.013>, URL <https://www.sciencedirect.com/science/article/pii/S003442571201824>.
- Ferretti, Alessandro, Monti-Guarnieri, Andrea, Prati, Claudio, Rocca, Fabio, Massonet, Didier, 2007. In: Fletcher, Karen (Ed.), InSAR Principles: Guidelines for SAR Interferometry Processing and Interpretation: Part3. In: TM-19, ESA Publications, ESTEC, Noordwijk, The Netherlands, ISBN: 92-9092-233-8, URL https://www.esa.int/esapub/tm/tm19/TM-19_ptC.pdf. Technical coordination by Juerg Lichtenegger, ESA/ESRIN (retired), Frascati, Italy.
- FloodList, News, 2023. Iran - floods in 3 provinces after heavy rain. <https://floodlist.com/asia/iran-floods-kerman-sistan-and-baluchestan-hormozgan-january-2020>. (Accessed 30 July 2023).
- Gabellini, Federica, 2021. When the desert becomes flooded. <https://unocha.exposure.co/when-the-desert-becomes-flooded>. (Accessed 04 December 2023).
- Garg, Shagun, Motagh, Mahdi, Indu, J., Karanam, Vamshi, 2022. Tracking hidden crisis in India's capital from space: Implications of unsustainable groundwater use. *Sci. Rep.* 12, 651. <http://dx.doi.org/10.1038/s41598-021-04193-9>.
- Geudtner, Dirk, Torres, Ramón, Snoeij, Paul, Davidson, Malcolm, Rommen, Björn, 2014. Sentinel-1 system capabilities and applications. In: 2014 IEEE Geoscience and Remote Sensing Symposium. pp. 1457–1460. <http://dx.doi.org/10.1109/IGARSS.2014.6946711>.

- Ghosh, Binayak, Garg, Shagun, Motagh, Mahdi, 2022. Automatic flood detection from sentinel-1 data using deep learning architectures. *ISPRS Ann. Photogramm. Remote Sens. Spat. Inf. Sci.* V-3-2022, 201–208. <http://dx.doi.org/10.5194/isprs-annals-V-3-2022-201-2022>, URL <https://isprs-annals.copernicus.org/articles/V-3-2022/201-2022/>.
- Ghosh, Binayak, Garg, Shagun, Motagh, Mahdi, Martinis, Sandro, 2024. Automatic flood detection from sentinel-1 data using a nested unet model and a NASA benchmark dataset. *PFG – J. Photogramm. Remote Sens. Geoinf. Sci.* (ISSN: 2512-2819) 92 (1), 1–18. <http://dx.doi.org/10.1007/s41064-024-00275-1>.
2024. Global seasonal sentinel-1 interferometric coherence and backscatter data set. <https://registry.opendata.aws/ebd-sentinel-1-global-coherence-backscatter>. (Accessed 15 July 2024).
- Gosiewska, Alicja, Kozak, Anna, Biecek, Przemysław, 2021. Simpler is better: Lifting interpretability-performance trade-off via automated feature engineering. *Decis. Support. Syst.* (ISSN: 0167-9236) 150, 113556. <http://dx.doi.org/10.1016/j.dss.2021.113556>, URL <https://www.sciencedirect.com/science/article/pii/S016792362100066X>. Interpretable Data Science For Decision Making.
- Haiqin, Cheng, Qiang, Chen, Guoxiang, Liu, Yinghui, Yang, 2013. A new method for SAR image coregistration from interferometric coherence modeling. In: Proceedings of the 2013 the International Conference on Remote Sensing, Environment and Transportation Engineering. RSETE 2013, Atlantis Press, ISBN: 978-90-78677-77-2, pp. 90–93. <http://dx.doi.org/10.2991/rsete.2013.23>.
- Hastie, T., Tibshirani, R., Friedman, J., 2009a. *Elements of Statistical Learning*, second ed. Springer, pp. 592–593.
- Hastie, Trevor, Tibshirani, Robert, Friedman, Jerome, 2009b. The Elements of Statistical Learning: Data Mining, Inference, and Prediction. In: Springer Series in Statistics, Springer New York, New York, NY, ISBN: 978-0-387-84857-0, <http://dx.doi.org/10.1007/978-0-387-84858-7>.
- Hein, Achim, 2004. SAR basics. In: Processing of SAR Data: Fundamentals, Signal Processing, Interferometry. Springer Berlin Heidelberg, Berlin, Heidelberg, ISBN: 978-3-662-09457-0, pp. 17–97. http://dx.doi.org/10.1007/978-3-662-09457-0_2.
- Hooker, Giles, Menth, Lucas, Zhou, Shengjia, 2021. Unrestricted permutation forces extrapolation: variable importance requires at least one more model, or there is no free variable importance. *Stat. Comput.* 31, 82. <http://dx.doi.org/10.1007/s11222-021-10057-z>.
- Ivan Ulloa, Noel, Chiang, Shou-Hao, Yun, Sang-Ho, 2020. Flood proxy mapping with normalized difference sigma-naught index and Shannon's entropy. *Remote Sens.* (ISSN: 2072-4292) 12 (9), URL <https://www.mdpi.com/2072-4292/12/9/1384>.
- Jo, M.-J., Osmanoglu, B., Zhang, B., Wdowinski, S., 2018. Flood extent mapping using dual-polarimetric sentinel-1 synthetic aperture radar imagery. *Int. Arch. Photogramm. Remote Sens. Spat. Inf. Sci.* XLII-3, 711–713. <http://dx.doi.org/10.5194/isprs-archives-XLII-3-711-2018>, URL <https://isprs-archives.copernicus.org/articles/XLII-3/711/2018/>.
- Karanam, Vamshi, Motagh, Mahdi, Garg, Shagun, Jain, Kamal, 2021. Multi-sensor remote sensing analysis of coal fire induced land subsidence in Jharia Coal-fields, Jharkhand, India. *Int. J. Appl. Earth Obs. Geoinf.* (ISSN: 1569-8432) 102, 102439. <http://dx.doi.org/10.1016/j.jag.2021.102439>, URL <https://www.sciencedirect.com/science/article/pii/S030324342100146X>.
- Karra, Krishna, Kontgis, Caitlin, Statman-Weil, Zoe, Mazzariello, Joseph C., Mathis, Mark, Brumby, Steven P., 2021. Global land use/land cover with sentinel 2 and deep learning. In: 2021 IEEE International Geoscience and Remote Sensing Symposium IGARSS. pp. 4704–4707. <http://dx.doi.org/10.1109/IGARSS47720.2021.9553499>, URL <https://ieeexplore.ieee.org/document/9553499>.
- Kellndorfer, Josef, Cartus, Oliver, Lavalle, Marco, Magnard, Christophe, Milillo, Pietro, Oveisgharan, Shadi, Osmanoglu, Batu, Rosen, Paul A., Wegmüller, Urs, 2022. Global seasonal sentinel-1 interferometric coherence and backscatter data set. *Sci. Data* 9 (1), 73. <http://dx.doi.org/10.1038/s41597-022-01189-6>.
- Korichi, K., Hazzab, A., Atallah, M., 2016. Flash floods risk analysis in ephemeral streams: a case study on Wadi Mekerra (northwestern Algeria). *Arab. J. Geosci.* 9, 589, URL <https://doi.org/10.1007/s12517-016-2624-2>.
- Krieger, Gerhard, Moreira, Alberto, Fiedler, Hauke, Hajnsek, Irena, Werner, Marian, Younis, Marwan, Zink, Manfred, 2007. TanDEM-X: A satellite formation for high-resolution SAR interferometry. *IEEE Trans. Geosci. Remote Sens.* 45 (11), 3317–3341. <http://dx.doi.org/10.1109/TGRS.2007.900693>.
- Krullikowski, Christian, Chow, Candace, Wieland, Marc, Martinis, Sandro, Bauer-Marschallinger, Bernhard, Roth, Florian, Matgen, Patrick, Chini, Marco, Hostache, Renaud, Li, Yu, Salomon, Peter, 2023. Estimating ensemble likelihoods for the sentinel-1 based global flood monitoring product of the copernicus emergency management service. [arXiv:2304.12488](https://arxiv.org/abs/2304.12488). URL <https://ieeexplore.ieee.org/stamp/stamp.jsp?arnumber=10186373>.
- Landuyt, Lisa, Van Wesemael, Alexandra, Schumann, Guy J.-P., Hostache, Renaud, Verhoest, Niko E.C., Van Coillie, Frieke M.B., 2019. Flood mapping based on synthetic aperture radar: An assessment of established approaches. *IEEE Trans. Geosci. Remote Sens.* (ISSN: 1558-0644) 57 (2), 722–739. <http://dx.doi.org/10.1109/TGRS.2018.2860054>.
- Lee, Jong-Sen, Wen, Jen-Hung, Ainsworth, T.L., Chen, Kun-Shan, Chen, A.J., 2009. Improved sigma filter for speckle filtering of SAR imagery. *IEEE Trans. Geosci. Remote Sens.* (ISSN: 1558-0644) 47 (1), 202–213.
- Li, Zhengxiao Tony, Bethel, James, 2008. Image coregistration in sar interferometry. URL <https://api.semanticscholar.org/CorpusID:248663>.
- Li, Yu, Martinis, Sandro, Plank, Simon, Ludwig, Ralf, 2018. An automatic change detection approach for rapid flood mapping in sentinel-1 SAR data. *Int. J. Appl. Earth Obs. Geoinf.* (ISSN: 1569-8432) 73, 123–135. <http://dx.doi.org/10.1016/j.jag.2018.05.023>, URL <https://www.sciencedirect.com/science/article/pii/S0303243418302782>.
- Li, Yu, Martinis, Sandro, Wieland, Marc, 2019. Urban flood mapping with an active self-learning convolutional neural network based on TerraSAR-X intensity and interferometric coherence. *ISPRS J. Photogramm. Remote Sens.* (ISSN: 0924-2716) 152, 178–191. <http://dx.doi.org/10.1016/j.isprsjprs.2019.04.014>, URL <https://www.sciencedirect.com/science/article/pii/S092427161930111X>.
- Li, Hui, Zhao, Jiayang, Yan, Bingqi, Yue, Linwei, Wang, Lunche, 2022. Global DEMs vary from one to another: an evaluation of newly released copernicus, NASA and AW3D30 DEM on selected terrains of China using ICESat-2 altimetry data. *Int. J. Digit. Earth* 15 (1), 1149–1168. <http://dx.doi.org/10.1080/17538947.2022.2094002>, arXiv:<https://doi.org/10.1080/17538947.2022.2094002>.
- Lin, Xiao, 1999. Flash Floods in Arid and Semi-Arid Zones. Technical Documents in Hydrology SC.99/WS/34, 23, UNESCO, p. 60, URL <https://unesdoc.unesco.org/ark:/48223/pf0000118882>. Incl. bibl.
- Lin, Yunung Nina, Yun, Sang-Ho, Bhardwaj, Alok, Hill, Emma M., 2019. Urban flood detection with sentinel-1 multi-temporal synthetic aperture radar (SAR) observations in a Bayesian framework: A case study for hurricane matthew. *Remote Sens.* (ISSN: 2072-4292) 11 (15), <http://dx.doi.org/10.3390/rs11151778>, URL <https://www.mdpi.com/2072-4292/11/15/1778>.
- Mahdavi, Sahel, Salehi, Bahram, Huang, Weimin, Amani, Meisam, Brisco, Brian, 2019. A PolSAR change detection index based on neighborhood information for flood mapping. *Remote Sens.* (ISSN: 2072-4292) 11 (16), <http://dx.doi.org/10.3390/rs11161854>, URL <https://www.mdpi.com/2072-4292/11/16/1854>.
- Martinis, Sandro, Kersten, Jens, Twele, André, 2015. A fully automated TerraSAR-X based flood service. *ISPRS J. Photogramm. Remote Sens.* (ISSN: 0924-2716) 104, 203–212. <http://dx.doi.org/10.1016/j.isprsjprs.2014.07.014>, URL <https://www.sciencedirect.com/science/article/pii/S0924271614001981>.
- Martinis, Sandro, Plank, Simon, Ćwik, Kamila, 2018. The use of sentinel-1 time-series data to improve flood monitoring in arid areas. *Remote Sens.* (ISSN: 2072-4292) 10 (4), <http://dx.doi.org/10.3390/rs10040583>, URL <https://www.mdpi.com/2072-4292/10/4/583>.
- Mason, D.C., Giustarini, L., Garcia-Pintado, J., Cloke, H.L., 2014. Detection of flooded urban areas in high resolution synthetic aperture radar images using double scattering. *Int. J. Appl. Earth Obs. Geoinf.* (ISSN: 1569-8432) 28, 150–159. <http://dx.doi.org/10.1016/j.jag.2013.12.002>, URL <https://www.sciencedirect.com/science/article/pii/S0303243413001700>.
- Maxwell, Aaron E., Warner, Timothy A., Fang, Fang, 2018. Implementation of machine-learning classification in remote sensing: an applied review. *Int. J. Remote Sens.* 39 (9), 2784–2817. <http://dx.doi.org/10.1080/01431161.2018.1433343>, arXiv:<https://doi.org/10.1080/01431161.2018.1433343>.
- Mirsoleiman, Hadi Rezaei, Sahebi, Mohammad Reza, Baghdadi, Nicolas, El Hajj, Mohamad, 2019. Bare soil surface moisture retrieval from sentinel-1 SAR data based on the calibrated IEM and dubois models using neural networks. *Sensors* 19 (14), 3209. <http://dx.doi.org/10.3390/s19143209>, URL <https://www.mdpi.com/1424-8220/19/14/3209>.
- Mohammadianesh, Fariba, Salehi, Bahram, Mahdianpari, Masoud, Brisco, Brian, Motagh, Mahdi, 2018a. Wetland water level monitoring using interferometric synthetic aperture radar (InSAR): A review. *Can. J. Remote Sens.* 44 (4), 247–262. <http://dx.doi.org/10.1080/07038992.2018.1477680>, arXiv:<https://doi.org/10.1080/07038992.2018.1477680>.
- Mohammadianesh, Fariba, Salehi, Bahram, Mahdianpari, Masoud, Brisco, Brian, Motagh, Mahdi, 2018b. Multi-temporal, multi-frequency, and multi-polarization coherence and SAR backscatter analysis of wetlands. *ISPRS J. Photogramm. Remote Sens.* (ISSN: 0924-2716) 142, 78–93. <http://dx.doi.org/10.1016/j.isprsjprs.2018.05.009>, URL <https://www.sciencedirect.com/science/article/pii/S0924271618301412>.
- Montello, Fabio, Arnaudo, Edoardo, Rossi, Claudio, 2022. Mmflood: A multimodal dataset for flood delineation from satellite imagery. <http://dx.doi.org/10.21227/bprf-jf62>.
- Motagh, M., Akhani, H., 2023. The cascading failure of check dam systems during the 28 july 2022 Emamzadeh Davood flood in Iran. *Nat. Hazards* 116, 4051–4057. <http://dx.doi.org/10.1007/s11069-023-05814-4>, URL <https://link.springer.com/article/10.1007/s11069-023-05814-4>.
- Network, Climate News, 2020. Drylands hit harder by poverty than richer regions. URL <https://www.preventionweb.net/quick/17801>. (Accessed 17 August 2023).
- Nico, G., Pappalepore, M., Pasquarello, G., Refice, A., Samarelli, S., 2000. Comparison of SAR amplitude vs. coherence flood detection methods - a GIS application. *Int. J. Remote Sens.* 21 (8), 1619–1631. <http://dx.doi.org/10.1080/014311600209931>, arXiv:<https://doi.org/10.1080/014311600209931>.
- Olen, Stephanie, Bookhagen, Bodo, 2020. Applications of SAR interferometric coherence time series: Spatiotemporal dynamics of geomorphic transitions in the south-central andes. *J. Geophys. Res.: Earth Surf.* 125 (3), e2019JF005141. <http://dx.doi.org/10.1029/2019JF005141>, URL <https://agupubs.onlinelibrary.wiley.com/doi/abs/10.1029/2019JF005141>, arXiv:<https://agupubs.onlinelibrary.wiley.com/doi/pdf/10.1029/2019JF005141>.

- Oshiro, Thais Mayumi, Perez, Pedro Santoro, Baranauskas, José Augusto, 2012. How many trees in a random forest? In: Perner, Petra (Ed.), Machine Learning and Data Mining in Pattern Recognition. Springer Berlin Heidelberg, Berlin, Heidelberg, ISBN: 978-3-642-31537-4, pp. 154–168.
- OTSU, Nobuyuki, 1979. A threshold selection method from gray-level histograms. *IEEE Trans. Syst. Man Cybern.* 9 (1), 62–66. <http://dx.doi.org/10.1109/TSMC.1979.4310076>.
- Pak Mission Society, 2020. Flood 2020 Pakistan. <https://pakmissionssociety.org/flood-2020-pakistan/>. (Accessed 30 July 2023).
- Panahi, Mahdi, Rahmati, Omid, Kalantari, Zahra, Darabi, Hamid, Rezaie, Fatemeh, Moghaddam, Davoudi, Ferreira, Carla Sofia Santos, Foody, Giles, Aliramee, Ramyar, Bateni, Sayed M., Lee, Chang-Wook, Lee, Saro, 2022. Large-scale dynamic flood monitoring in an arid-zone floodplain using SAR data and hybrid machine-learning models. *J. Hydrol.* (ISSN: 0022-1694) 611, 128001. <http://dx.doi.org/10.1016/j.jhydrol.2022.128001>, URL <https://www.sciencedirect.com/science/article/pii/S0022169422005765>.
- Peyravi, M., Peyvandi, A.A., Khodadadi, A., Ahmadi Marzaleh, M., 2019. Flood in the south-west of Iran in 2019; causes, problems, actions and lesson learned. *Bull. Emerg. Trauma* 7 (2), 199–200. <http://dx.doi.org/10.29252/beat-070219>, URL <https://pubmed.ncbi.nlm.nih.gov/31198813/>. PMID: 31198813; PMCID: PMC6555208.
- Piantanida, R., Miranda, N., Franceschi, N., Meadows, P., 2017. Thermal Denoising of Products Generated by the S-1 IPF. Tech. Rep. MPC-0392, Sentinel-1 Mission Perform. Centre, Ramonville-Saint-Agne, France, URL <https://sentinels.copernicus.eu/documents/247904/2142675/Thermal-Denoising-of-Products-Generated-by-Sentinel-1-IPF.pdf>.
- Preiss, Mark, Stacy, Nick J.S., 2006. Coherent change detection: Theoretical description and experimental results. URL <https://api.semanticscholar.org/CorpusID:129535374>.
- Prigent, Catherine, Aires, Filipe, Jimenez, Carlos, Papa, Fabrice, Roger, Jack, 2015. Multiangle backscattering observations of continental surfaces in ku-band (13 GHz) from satellites: Understanding the signals, particularly in arid regions. *IEEE Trans. Geosci. Remote Sens.* (ISSN: 1558-0644) 53 (3), 1364–1373. <http://dx.doi.org/10.1109/TGRS.2014.2338913>.
- Probst, Philipp, Wright, Marvin N., Boulesteix, Anne-Laure, 2019. Hyperparameters and tuning strategies for random forest. *WIREs Data Min. Knowl. Discov.* 9 (3), e1301. <http://dx.doi.org/10.1002/widm.1301>, URL <https://wires.onlinelibrary.wiley.com/doi/abs/10.1002/widm.1301>. arXiv:<https://wires.onlinelibrary.wiley.com/doi/pdf/10.1002/widm.1301>.
- Pulvirenti, Luca, Chini, Marco, Pierdicca, Nazzareno, Boni, Giorgio, 2016. Use of SAR data for detecting floodwater in urban and agricultural areas: The role of the interferometric coherence. *IEEE Trans. Geosci. Remote Sens.* 54 (3), 1532–1544. <http://dx.doi.org/10.1109/TGRS.2015.2482001>.
- Pulvirenti, Luca, Marzano, Frank Silvio, Pierdicca, Nazzareno, Mori, Saverio, Chini, Marco, 2014. Discrimination of water surfaces, heavy rainfall, and wet snow using COSMO-SkyMed observations of severe weather events. *IEEE Trans. Geosci. Remote Sens.* 52 (2), 858–869. <http://dx.doi.org/10.1109/TGRS.2013.2244606>, URL <https://ieeexplore.ieee.org/document/6488761>.
- Rambour, Clément, Audebert, Nicolas, Koeniguer, Elise, Le Saux, Bertrand, Crucianu, Michel, Datcu, Mihai, 2020. SEN12-FLOOD : a SAR and multispectral dataset for flood detection. <http://dx.doi.org/10.21227/w6xz-s898>.
- Reffice, Alberto, Capolongo, Domenico, Pasquariello, Guido, D'Addabbo, Annarita, Bovena, Fabio, Nutricato, Raffaele, Lovergine, Francesco P., Pietranera, Luca, 2014. SAR and InSAR for flood monitoring: Examples with COSMO-SkyMed data. *IEEE J. Sel. Top. Appl. Earth Obs. Remote Sens.* (ISSN: 2151-1535) 7 (7), 2711–2722. <http://dx.doi.org/10.1109/JSTARS.2014.2305165>, URL <https://ieeexplore.ieee.org/document/6758381>.
- Rentschler, J., Salhab, M., Jafino, B.A., 2022. Flood exposure and poverty in 188 countries. *Nature Commun.* 13 (1), 3527. <http://dx.doi.org/10.1038/s41467-022-30727-4>, URL <https://www.ncbi.nlm.nih.gov/pmc/articles/PMC9240081/>.
- Ritushree, DK, Garg, Shagun, Dasgupta, Antara, Martinis, Sandro, Selvamaran, Sivasakthy, Motagh, Mahdi, 2023. Improving SAR-based flood detection in arid regions using texture features. In: 2023 International Conference on Machine Intelligence for GeoAnalytics and Remote Sensing. MIGARS, Vol. 1, pp. 1–4. <http://dx.doi.org/10.1109/MIGARS57353.2023.10064526>, URL <https://ieeexplore.ieee.org/document/10064526>.
- Santoro, Maurizio, Askne, Jan I.H., Wegmüller, Urs, Werner, Charles L., 2007. Observations, modeling, and applications of ERS-ENVISAT coherence over land surfaces. *IEEE Trans. Geosci. Remote Sens.* 45 (8), 2600–2611. <http://dx.doi.org/10.1109/TGRS.2007.897420>.
- Santoro, Maurizio, Wegmüller, Urs, Askne, Jan I.H., 2010. Signatures of ERS-ENVISAT interferometric SAR coherence and phase of short vegetation: An analysis in the case of maize fields. *IEEE Trans. Geosci. Remote Sens.* 48 (4), 1702–1713. <http://dx.doi.org/10.1109/TGRS.2009.2034257>, URL <https://ieeexplore.ieee.org/document/5357427>.
- Schaber, Gerald G., McCauley, John F., Breed, Carol S., Olhoeft, Gary R., 1986. Shuttle imaging radar: Physical controls on signal penetration and subsurface scattering in the eastern sahara. *IEEE Trans. Geosci. Remote Sens.* (ISSN: 1558-0644) GE-24 (4), 603–623. <http://dx.doi.org/10.1109/TGRS.1986.289677>.
- Schepanski, K., Wright, T.J., Knippertz, P., 2012. Evidence for flash floods over deserts from loss of coherence in insar imagery. *J. Geophys. Res.: Atmos.* 117 (D20), <http://dx.doi.org/10.1029/2012JD017580>, URL <https://agupubs.onlinelibrary.wiley.com/doi/abs/10.1029/2012JD017580>. arXiv:<https://agupubs.onlinelibrary.wiley.com/doi/pdf/10.1029/2012JD017580>.
- Schlaffer, Stefan, Matgen, Patrick, Hollaus, Markus, Wagner, Wolfgang, 2015. Flood detection from multi-temporal SAR data using harmonic analysis and change detection. *Int. J. Appl. Earth Obs. Geoinf.* (ISSN: 1569-8432) 38, 15–24. <http://dx.doi.org/10.1016/j.jag.2014.12.001>, URL <https://www.sciencedirect.com/science/article/pii/S0303243414002645>.
- Schumann, Guy, Giustarini, Laura, Tarpanelli, Angelica, Jarihani, Ben, Martinis, Sandro, 2022. Flood modeling and prediction using earth observation data - surveys in geophysics. URL <https://link.springer.com/article/10.1007/s10712-022-09751-y>.
- Scornet, Erwan, 2017. Tuning parameters in random forests. *ESAIM: Procs* 60, 144–162. <http://dx.doi.org/10.1051/proc/201760144>.
- Sentinel-Asia, 2023. Sentinel-Asia. <https://sentinel-asia.org/>. (Accessed 06 October 2023).
- Smiljanic, Ivan, Kerkmann, Jochen, Lancaster, Sancha, 2019. Widespread flooding in the middle east. <https://www.eumetsat.int/widespread-flooding-middle-east>. (Accessed 30 July 2023).
- Tabari, Hossein, 2020. Climate change impact on flood and extreme precipitation increases with water availability. *Sci. Rep.* 10, 13768. <http://dx.doi.org/10.1038/s41598-020-70816-2>.
- Tay, Cheryl W.J., Yun, Sang-Ho, Chin, Shi Tong, Bhardwaj, Alok, Jung, Jungkyo, Hill, Emma M., 2020. Rapid flood and damage mapping using synthetic aperture radar in response to Typhoon Hagibis, Japan. *Sci. Data* 7, 100. <http://dx.doi.org/10.1038/s41597-020-0443-5>, URL <https://www.nature.com/articles/s41597-020-0443-5>.
- Tellman, B., Sullivan, J.A., Kuhn, C., Kettner, A.J., Doyle, C.S., Brakenridge, G.R., Erickson, T.A., Slayback, D.A., 2021. Satellite imaging reveals increased proportion of population exposed to floods. *Nature* 596, 80–86. <http://dx.doi.org/10.1038/s41586-021-03695-w>.
- Toca, L., Morrison, K., Artz, R.R.E., Gimona, A., Quaife, T., 2022. High resolution C-band SAR backscatter response to peatland water table depth and soil moisture: a laboratory experiment. *Int. J. Remote Sens.* 43 (14), 5231–5251. <http://dx.doi.org/10.1080/01431161.2022.2131478>. arXiv:<https://doi.org/10.1080/01431161.2022.2131478>.
- Touzi, R., Lopes, A., Bruniquel, J., Vachon, P.W., 1999. Coherence estimation for SAR imagery. *IEEE Trans. Geosci. Remote Sens.* 37 (1), 135–149. <http://dx.doi.org/10.1109/36.739146>, URL <https://ieeexplore.ieee.org/document/739146>.
- Twete, André, Cao, Wenxi, Plank, Simon, Martinis, Sandro, 2016. Sentinel-1-based flood mapping: a fully automated processing chain. *Int. J. Remote Sens.* 37 (13), 2990–3004. <http://dx.doi.org/10.1080/01431161.2016.1192304>.
- Ulaby, Fawwaz T., Battlivala, Percy P., Dobson, Myron C., 1978. Microwave backscatter response on surface roughness, soil moisture, and soil texture: Part I-Bare soil. *IEEE Trans. Geosci. Electron.* (ISSN: 0018-9413) 16 (4), 286–295. <http://dx.doi.org/10.1109/TGE.1978.294586>.
- Ulaby, Fawwaz T., Dubois, Pascale C., van Zyl, Jakob, 1996. Radar mapping of surface soil moisture. *J. Hydrol.* (ISSN: 0022-1694) 184 (1), 57–84. [http://dx.doi.org/10.1016/0022-1694\(95\)02968-0](http://dx.doi.org/10.1016/0022-1694(95)02968-0), URL <https://www.sciencedirect.com/science/article/pii/0022169495029680>. Soil Moisture Theories and Observations.
- Vanama, Venkata Sai Krishna, Mandal, Dipankar, Rao, Yalamanchili S., 2020. GEE4FLOOD: rapid mapping of flood areas using temporal sentinel-1 SAR images with google earth engine cloud platform. *J. Appl. Remote Sens.* 14 (3), 034505. <http://dx.doi.org/10.1117/1.JRS.14.034505>.
- Vanama, Venkata Sai Krishna, Mustafa, Mohamed Saiyad, Khati, Unmesh, Gowtham, Ramasamy, Singh, Gulab, Rao, Yalamanchili Subrahmanyaswara, 2021b. Inundation mapping of kerala flood event in 2018 using ALOS-2 and temporal sentinel-1 SAR images. URL <https://api.semanticscholar.org/CorpusID:235351714>.
- Vanama, V.S.K., Rao, Y.S., Bhatt, C.M., 2021a. Change detection based flood mapping using multi-temporal earth observation satellite images: 2018 flood event of Kerala, India. *Eur. J. Remote Sens.* 54 (1), 42–58. <http://dx.doi.org/10.1080/22797254.2020.1867901>. arXiv:<https://doi.org/10.1080/22797254.2020.1867901>.
- Villarroyo-Carpio, Arturo, Lopez-Sánchez, Juan M., Engdahl, Marcus E., 2022. Sentinel-1 interferometric coherence as a vegetation index for agriculture. *Remote Sens. Environ.* (ISSN: 0034-4257) 280, 113208. <http://dx.doi.org/10.1016/j.rse.2022.113208>, URL <https://www.sciencedirect.com/science/article/pii/S0034425722003169>.
- Wagner, W., 2024. Scientific challenges when using SAR images for mapping of water bodies and floods everywhere and anytime. In: EGU General Assembly 2024. In: EGU24-8642, Vienna, Austria, <http://dx.doi.org/10.5194/egusphere-egu24-8642>.
- Wagner, Wolfgang, Hahn, Sebastian, Kidd, Richard, Melzer, Thomas, Bartalis, Zoltan, Hasenauer, Stefan, Figal-Saldana, Julia, de Rosnay, Patricia, Jann, Alexander, Schneider, Stefan, Komma, Jürgen, Kubu, Gerhard, Brugger, Katharina, Aubrecht, Christoph, Züger, Johann, Gangkofner, Ute, Kienberger, Stefan, Brocca, Luca, Wang, Yong, Blöschl, Günter, Eitzinger, Josef, Steinnocher, Kla, 2013. The ASCAT soil moisture product: A review of its specifications, validation results, and emerging applications. *Meteorol. Z.* 22 (1), 5–33. <http://dx.doi.org/10.1127/0941-2948/2013/0399>.

- Wagner, Wolfgang, Lindorfer, Roland, Melzer, Thomas, Hahn, Sebastian, Bauer-Marschallinger, Bernhard, Morrison, Keith, Calvet, Jean-Christophe, Hobbs, Stephen, Quast, Raphael, Greimeister-Pfeil, Isabella, Vreugdenhil, Mariette, 2022. Widespread occurrence of anomalous C-band backscatter signals in arid environments caused by subsurface scattering. *Remote Sens. Environ.* (ISSN: 0034-4257) 276, 113025. <http://dx.doi.org/10.1016/j.rse.2022.113025>, URL <https://www.sciencedirect.com/science/article/pii/S0034425722001390>.
- Wang, Teng, Liao, Mingsheng, Perissin, Daniele, 2010. InSAR coherence-decomposition analysis. *IEEE Geosci. Remote Sens. Lett.* 7 (1), 156–160. <http://dx.doi.org/10.1109/LGRS.2009.2029126>, URL <https://ieeexplore.ieee.org/document/5263020>.
- Wegmüller, Urs, 1999. Automated terrain corrected SAR geocoding. In: IEEE Geoscience and Remote Sensing Symposium. IEEE, Hamburg, pp. 1712–1714, URL <https://ieeexplore.ieee.org/stamp/stamp.jsp?arnumber=772070>.
- Wendleder, Anna, Wessel, Birgit, Roth, Achim, Breunig, Markus, Martin, Klaus, Wagenbrenner, Susanne, 2013. TanDEM-X water indication mask: Generation and first evaluation results. *IEEE J. Sel. Top. Appl. Earth Obs. Remote Sens.* 6 (1), 171–179. <http://dx.doi.org/10.1109/JSTARS.2012.2210999>, URL <https://ieeexplore.ieee.org/document/6303842>.
- Wieland, Marc, Martinis, Sandro, Kiefl, Ralph, Gstaiger, Veronika, 2023. Semantic segmentation of water bodies in very high-resolution satellite and aerial images. *Remote Sens. Environ.* (ISSN: 0034-4257) 287, 113452. <http://dx.doi.org/10.1016/j.rse.2023.113452>, URL <https://www.sciencedirect.com/science/article/pii/S0034425723000032>.
- Wu, Lianhui, Tajima, Yoshimitsu, Yamanaka, Yusuke, Shimozono, Takenori, Sato, Shinji, 2019. Study on characteristics of SAR imagery around the coast for shoreline detection. *Coast. Eng. J.* 61 (2), 152–170. <http://dx.doi.org/10.1080/21664250.2018.1560685>, arXiv:<https://doi.org/10.1080/21664250.2018.1560685>.
- Wu, Xuan, Zhang, Zhijie, Xiong, Shengqing, Zhang, Wanchang, Tang, Jiakui, Li, Zheng-hao, An, Bangsheng, Li, Rui, 2023. A near-real-time flood detection method based on deep learning and SAR images. *Remote Sens.* (ISSN: 2072-4292) 15 (8), URL <https://www.mdpi.com/2072-4292/15/8/2046>.
- Xu, Hanqiu, 2006. Modification of normalised difference water index (NDWI) to enhance open water features in remotely sensed imagery. *Int. J. Remote Sens.* 27 (14), 3025–3033. <http://dx.doi.org/10.1080/01431160600589179>.
- Yadav, Ritu, Nascetti, Andrea, Ban, Yifang, 2022a. Attentive dual stream siamese U-net for flood detection on multi-temporal sentinel-1 data. In: IGARSS 2022 - 2022 IEEE International Geoscience and Remote Sensing Symposium. pp. 5222–5225, URL <https://ieeexplore.ieee.org/stamp/stamp.jsp?arnumber=9883132>.
- Yadav, Ritu, Nascetti, Andrea, Ban, Yifang, 2022b. Deep attentive fusion network for flood detection on uni-temporal sentinel-1 data. *Front. Remote Sens.* (ISSN: 2673-6187) 3, <http://dx.doi.org/10.3389/frsen.2022.1060144>, URL <https://www.frontiersin.org/articles/10.3389/frsen.2022.1060144>.
- Yang, Liping, Feng, Xiaodong, Liu, Fei, Liu, Jing, Sun, Xiaohui, 2019. Potential of soil moisture estimation using C-band polarimetric SAR data in arid regions. *Int. J. Remote Sens.* 40 (5–6), 2138–2150. <http://dx.doi.org/10.1080/01431161.2018.1516320>, arXiv:<https://doi.org/10.1080/01431161.2018.1516320>.
- Zhao, Jie, Li, Yu, Matgen, Patrick, Pelich, Ramona, Hostache, Renaud, Wagner, Wolfgang, Chini, Marco, 2022. Urban-aware U-net for large-scale urban flood mapping using multitemporal sentinel-1 intensity and interferometric coherence. *IEEE Trans. Geosci. Remote Sens.* 60, 1–21. <http://dx.doi.org/10.1109/TGRS.2022.3199036>, URL <https://ieeexplore.ieee.org/document/9857936>.
- Zhao, Jie, Pelich, Ramona, Hostache, Renaud, Matgen, Patrick, Cao, Senmao, Wagner, Wolfgang, Chini, Marco, 2021. Deriving exclusion maps from C-band SAR time-series in support of floodwater mapping. *Remote Sens. Environ.* (ISSN: 0034-4257) 265, 112668. <http://dx.doi.org/10.1016/j.rse.2021.112668>, URL <https://www.sciencedirect.com/science/article/pii/S0034425721003886>.
- Zhao, Jie, Xiong, Zhitong, Zhu, Xiao Xiang, 2024. UrbanSARfloods: Sentinel-1 SLC-based benchmark dataset for urban and open-area flood mapping. URL <https://arxiv.org/abs/2406.04111>, arXiv:2406.04111.